Photometric Study of the Globular Cluster System of M49

Aisha Mahmoud-Perez

A thesis presented for the degree of Master of Science

Department of Physics & Astronomy, McMaster University
July 2015

Aisha Mahmoud-Perez
Department of Physics and Astronomy, McMaster University
Hamilton, ON, Canada

Photometric Study of the M49 Globular Cluster System
Master's Thesis. 84 pages. July 16, 2015

Thesis Committee Members:
Dr. William E. Harris (Advisor)
Dr. Laura Parker
Dr. Alison Sills

This thesis presents deep photometry of the globular cluster system of the massive elliptical galaxy, M49. Using the C and T1 Washington filters from the MOSAIC camera on the Cerro Tololo Inter-American Observatory 4m telescope, we studied the color, metallicity and luminosity distributions of the globular cluster system.

We find a strong bimodality in the color and metallicity distributions of the globular cluster system down to a magnitude of R <24, with 1718 clusters belonging to the blue population and 698 to the red population. In agreement with previous studies, the blue sequence does not exhibit a strong mass-metallicity relation. No difference is found in the mass-metallicity relation between the inner and outer clusters of M49.

These results suggest that the mechanism responsible for the mass-metallicity relation is not local and may be affected by the galaxy's individual dynamic history, location in the galaxy cluster and the formation of the globular cluster system itself. We suggest a mechanism based on accretion of gas by proto-clusters as they orbit within their parent dwarf galaxies. The latter would fit the observed behavior of the MMR.

Keywords: globular cluster system, MMR, elliptical galaxies, accretion, metallicity

List of Abbreviations

BH: Bondi & Hoyle (1944)

CCD: Charged Coupled Device

CMD: Color-Magnitude Diagram

CTIO: Cerro Tololo Inter-American Observatory

EM: Expectation-Maximization

gE: Giant Elliptical Galaxies

FC: Fornax Cluster

FOV: Field of View

GCs: Globular Clusters

GCS: Globular Cluster System

GCLF: Globular Cluster Luminosity Function

GMM: Gaussian Mixture Model

HST: Hubble Space Telescope

IRAF: Image Reduction and Analysis Facility

MMR: Mass-Metallicity Relation

MW: Milky Way

Myr/Gyr: Mega-year/Giga-year

PSF: Point Spread Function

SNe: Supernovae

VC: Virgo Cluster

List of Figures

List of Tables

Contents

Chapter 1

Introduction

"...What do you mean, you've never been to Alpha Centauri? For heaven's sake, mankind, it's only four light-years away, you know..."
-Douglas Adams, *The Hitchhikers Guide to the Galaxy*

1.1 Globular Clusters

Globular Clusters (GCs) are massive objects containing anything from a few thousand to millions of stars; see figure 1.1. These families of stars form in rich molecular clouds. GCs are close to some of the oldest objects in the universe. Typical masses of these systems lie between 10^4 - 10^6 $M_\odot$ corresponding to luminosities of roughly M_v = -5 to -10 (Brodie and Strader (2006a)). GCs are high density environments; most of their mass is concentrated within a volume of roughly $\sim 10^3$ pc^3.

GCs can be found in galaxies of all morphologies brighter than $\sim M_B$ = -15. The number of GCs per galaxy varies significantly with massive elliptical galaxies (gE) harboring more GCs than their spiral, irregular or dwarf galaxy counterparts. The number of GCs formed is proportional to the halo mass of the galaxy (W. E. Harris, Harris, and Hudson (2015)); hence, gE are able to host a higher number of clusters. The Milky Way has about 150 GC (W. E. Harris (1996), W. E. Harris, Harris, and Alessi (2013)), the Fornax dwarf spheroidal has 5GC (Kissler-Patig et al. (1997)), while M87, a giant elliptical, has over 13,000 GC (Ashman 1998).

Figure 1.1: Globular Cluster M14. Credits: Robert Gensler

1.1.1 Globular Cluster Systems

While individual GCs are an area of interest in their own right, it is also interesting to study all GCs belonging to one galaxy collectively; mainly, to study the globular cluster *system* of the galaxy (GCS). In a typical gE, most of these GCs are old objects with ages around $\geq$10 Gyr.

When considered as a system, GCs can offer a window to their host galaxy's history. Since GCs are the oldest surviving objects of the formation and later evolution of their host galaxy, they offer a unique gateway to the dynamical history of the galaxy. The relative number of GCs per unit magnitude gives the globular cluster luminosity function (GCLF). The GCLF has been shown to follow a Gaussian, t-distribution or, more recently, a Schechter function (Secker (1992)).

Also, given the high number of stars present in any given globular cluster, they provide a good environment to study star formation and evolution and more exotic types of stars like blue stragglers or low-mass X-ray binaries. GCSs truly are massive laboratories for stellar phenomena. GCSs are unique relics and having a good understanding of them can provide powerful insights to the most fundamental aspects of both stellar and galaxy formation and evolution.

1.2 Bimodality in Globular Clusters

One of the most significant discoveries of the past 20 years with respect to GCS was the discovery of an apparent bimodality in their color distribution.

Early evidence for bimodality was noted by Couture, Harris, and Allwright (1990) and G. L. H. Harris, Geisler, Harris, and Hesser (1992) when using B-I CFHT imaging of NGC 4472. To some extent, this multimodality is related to the age of the object, but it likely translates into a bimodality in the abundance of heavy elements such as iron. It is known that there is a degeneracy between age and metallicity (Worthey (1994)). This degeneracy implies that both the spectroscopic and the photometric properties of the clusters in a young system are difficult to distinguish from a system several times older; mainly, a young metal-rich cluster is hard to distinguish from an old metal-poor cluster. Worthey (1994) noted that several spectral lines were particularly sensitive to age (Hydrogen lines) whereas metal lines were sensitive to metallicity. Hence, the definite cause of this multimodality cannot be attributed directly to age. Further spectroscopic research in this area, strongly links multimodality to different metallicities among the subpopulations of the GCSs (Woodley and Harris (2011), Puzia, Kissler-Patig, and Goudfrooij (2005), Strader, Brodie, Spitler, and Beasley (2006)). The most common form of multimodality among GCSs is a strong bimodality with one population being metal-poor (blue) and another being metal-rich(red), see figure 1.2. Signs of bimodality in metallicity have been observed in the

Milky Way (MW) as well as in M31 (Barmby (2000)). According to Zinn (1985), two different groups have been identified in the MW: "halo" metal-poor clusters and "disk" or "bulge" metal-rich clusters. GC subpopulations in other spirals are not as well defined as for the MW mainly due to contamination from young clusters and extinction correction problems. It is easier to study and observe bimodality in massive early-type galaxies because of the large number of GCs in their halos and no major issues involving extinction.

Several studies have looked into the early formation of the galaxy to try to account for the apparent bimodality. The major merger model proposed by Ashman and Zepf (1992) was a pioneer in the area since it predicted bimodality before it was observed. This model stated that new GCs were formed in gas-rich mergers of spiral galaxies resulting in a new elliptical galaxy made up of old metal-poor clusters and new metal-rich clusters. While it is an attractive model, a major argument against it is the inconsistency of the number and color distribution of the GCSs in massive elliptical galaxies simulations versus the observed data (Forbes, Brodie, and Grillmair (1997)).

Forbes et al. (1997) used a different approach and suggested a dissipational collapse model to explain bimodality. This model states that the metal-poor and metal-rich clusters formed in different modes of formation. In this multiphase dissipational collapse model, metal-poor GCs formed first in low-mass proto-galaxies between redshifts of 5 and 12. Soon after star-formation halts and when star-formation resumes and gas recollapses, metal-rich clusters are formed. Hence, this model produces two sub-populations of GC with different metallicities.

A dissipationless accretion model was also put forward to explain bimodality. This model suggests that the metal-rich cluster population forms in-situ in a massive seed galaxy whereas the metal-poor cluster population formed in the dissipationless accretion of nearby lower-mass galaxies (Côté, Marzke, and West (1998)). For this model to be successful a significant number of metal-poor field stars and metal-poor GCs must be accreted by the galaxy. The latter could be resolved by adding gas to the system or having the events occur at higher redshifts (Brodie et al. (2012)).

Most of these models suggest different formation epochs for the blue and red GCs. Muratov and Gnedin (2010) and Li and Gnedin (2014) suggested that bimodality arises naturally as the result of a small number of late massive merger events instead of different modes of formation for each subpopulation of clusters in the GCSs.

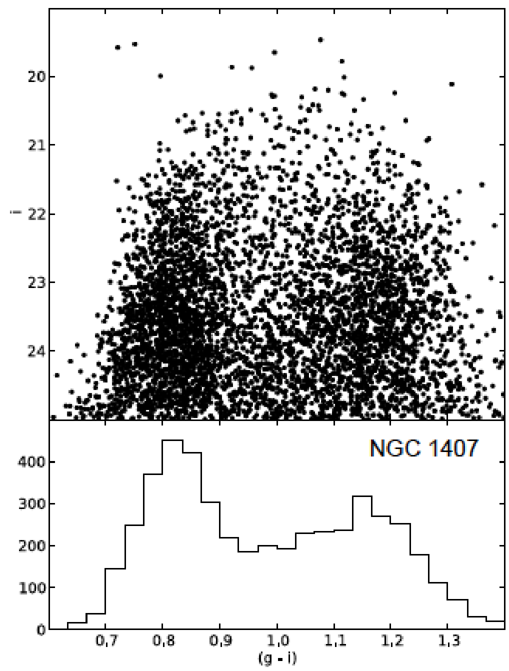

Figure 1.2: Top: Color-Magnitude Diagram of NGC 1407. Color bimodality can be seen in both the scatter and histogram plots. There are two very well defined peaks in color Bottom: CMD binned by color. Forbes et al. (2005)

1.3 The Underlying Shape of the Color Bimodality Distribution

Much of the current debate revolves around understanding what causes multimodality in GCSs. It has been suggested that if the relation between color and metallicity is not linear, a broad, single-peaked metallicity distribution that has been directly affected by continuous chemical enrichment can produce color bimodality in one single population (Richtler 2006, Yoon et al. 2011). The latter implies that this bimodality in the color distribution does not have to translate into a bimodality in the abundance of heavy elements. M31 is an example of a possible non-linear bimodal distribution. According to Kim et al. (2013), the bimodality in M31 might not be a direct result of age or metallicity, but rather a non-linear function of GC metallicity arising from the difference in the hot HB proportion of stellar populations in metal-poor GCs.

Globular cluster colors are an integrated projection of their spectral slopes. Recent spectroscopy has shown that most globular clusters are old and it is metallicity, not age, that is the main parameter influencing the observed color distribution (Forbes and Forte (2001); Brodie et al. (2005); Cenarro, Beasley, Strader, Brodie, and Forbes (2007), Woodley et al. (2010)). For simplicity, conversions between color and metallicity have been linear or quadratic fits (W. E. Harris and Harris (2002); Cohen, Blakeslee, and Côté (2003)). Contrasting scenarios have been recently put forward with the claim that the relation between color and metallicity is firmly non-linear (Yoon, Lee, Yi, and Lee (2006), Blakeslee, Cantiello, and Peng (2010)).

The idea that bimodal color histograms correspond to bimodal metallicity distributions comes directly from the assumption that optical colors are simple linear transformations of metallicity. While this is a reasonable assumption, since the mean colors of the main source of optical light in GCs are bright giant branch stars whose colors are strongly correlated with metallicity, if one is interested in the detailed shape of the metallicity distribution, a more in-depth examination of the color-metallicity relation is needed. An earlier indication of a possible nonlinearity between color and metallicity was put forward by W. E. Harris and Harris (2002) and was further extended by Yoon et al. (2006) who concentrated on (g-z) colors and stated that a nonlinear correlation between color and metallicity could potentially produce bimodality in color from a unimodal metallicity distribution.

Peng et al. (2006) also confirmed the possibility of a nonlinear relationship when they found a nonlinear color-metallicity transformation between g - z and [Fe/H] using *HST* data to study 100 massive elliptical galaxies in the Virgo cluster. Along similar lines, it was found that the color dispersion of the metal-rich subpopulation is significantly larger than that of the metal-poor subpopulation (Peng et al. (2006), Strader et al. (2006), W. E. Harris et al. (2006)). The color-metallicity relations adopted by the various papers in the literature led to different color dispersions in the color distributions of these populations. For example, W. E. Harris et al. (2006) used a linear fit betwen (B-I) and metallicity and Peng et al. (2006) used a piecewise linear relation in (g-z) to [Fe/H], but these were less certain at extreme colors. While the numerical value of the dispersion varied significantly between the two works, both found that the spread in the metal-poor population is smaller than that of the metal-rich population. The connection between these differences and the formation and enrichment histories of the galaxies is not yet understood.

Yoon et al. (2006) found that the color values for 150 GCs in M87 obtained from Cohen and Blakeslee (1998) follow a Gaussian metallicity distribution using their nonlinear conversions from color to metallicity; however, this only represents a fraction of the globular cluster population of the galaxy. Using Lick indexes, tools to derive the mean stellar population characteristics through the evolutionary synthesis of integrated spectra, for 47 GCs in M49, Strader, Beasley, and Brodie (2007) found that color-metallicity distributions strongly favor a bimodal Gaussian over a unimodal fit. It seems clear then that a linear fit is a reasonable assumption to a first degree order, but not optimal. In addition, this relationship depends on which color index is used. The exact shape of the relation between color and metallicity is still poorly understood. Nevertheless, even if the main catalyst for the apparent color bimodality is indeed of nonlinear origin, this does not rule out the possibility of multiple populations in massive galaxies. Subsequent works in the area looked into the GCSs of NGC 3115 and concluded that both color and the CaT index (calcium triplet) are strongly bimodal (Brodie et al. (2012)). On the basis of the evidence currently available, it seems fair to suggest that multiple globular cluster metallicity subpopulations are not uncommon.

1.4 The Mass-Metallicity Relation

The idea of globular clusters as simple and unimodal objects is now long gone. Besides a clear bimodality in almost all the GCSs of massive galaxies, a likely relationship between the luminosity and metallicity of the metal-poor globular clusters GCS has been observed.

This mass-metallicity relation (MMR), sometimes referred to as the 'blue tilt', shows that as the metal-poor clusters become more luminous (or more massive), they become increasingly more metal-rich, see figure 1.3. This phenomenon was first found by W. E. Harris et al. (2006) and by Strader et al. (2006) in massive elliptical galaxies, but has since been observed in various spirals as well (Spitler et al. (2006), W. E. Harris, Spitler, Forbes, and Bailin (2010)). According to Bailin and Harris (2009), the MMR becomes noticeable at masses of roughly $\sim 10^6\ M_{\odot}$. Due to the merging of the blue and red peaks at the brightest magnitudes, and the small number of very luminous GCs present, the precise behavior of the blue tilt at the bright end is still unclear.

The MMR is parameterized by Z $\sim M^{\alpha}$, where Z is the GC heavy-element abundance, M is the GC mass and α is the slope of the MMR. Mass estimates are obtained by assuming a constant mass-to-luminosity ratio, whereas Z is calculated from the observed data using color-metallicity conversions. Given the variety of filters used to observe GCSs and measure the MMR, there are several conversion relations between color and metallicity; consequently, uncertainties can arise in the measured slopes; nevertheless, a simple, single power-law model favors the observed data of globular clusters above a mass of $10^6\ M_{\odot}$.

One of the main difficulties in detecting the MMR is that the MMR slopes are fairly small; hence, unless a large GC sample is available, the chances of observing this relation are slim. In addition, precise photometric studies are needed in order to observe the MMR and such samples were not available until recent years. Kundu (2008) suggested that the MMR phenomenon could simply be a result of aperture photometry, low signal-to-noise ratio and a mass-radius relation for globular clusters. However, several studies with both ground- and space-based observations and different photometric techniques have confirmed the existence of the MMR (W. E. Harris (2009); W. E. Harris et al. (2006); Mieske et al. (2010); Strader et al. (2006)).

It is no surprise that most MMRs have been observed in gEs since they possess bigger potentials than their spiral counterparts enabling them to harbor more GCs. However, there are cases, like the massive elliptical M49, where the galaxy was claimed not to exhibit an MMR (Strader et al. (2006)). If the absence of an MMR is confirmed, this would imply that there is no *universal* model to explain this new phenomenon in massive galaxies. An important factor in whether a galaxy will exhibit an MMR, is both the number of clusters the galaxy can host and the luminosity/mass of the members of the GCS. Only the most massive, most luminous clusters will be affected by the MMR. It has also been suggested that the individual dynamical history of the galaxy could play a potential role in the formation of the MMR (Mieske et al. (2006)).

1.4.1 Several Cases of the MMR

There is a rapidly growing literature on the discovery on the MMR in different types of galaxies. This section discusses some of the cases discovered to date.

The MMR in Massive Elliptical Galaxies

Massive elliptical galaxies are the most natural environments for GCSs. These galaxies have GCs that may number in the thousands. GCSs are also easier to study in the environment of gEs since no problems arise with internal reddening or confusing disk objects. Hence, gE are the long-standing face of studies for the MMR. Table

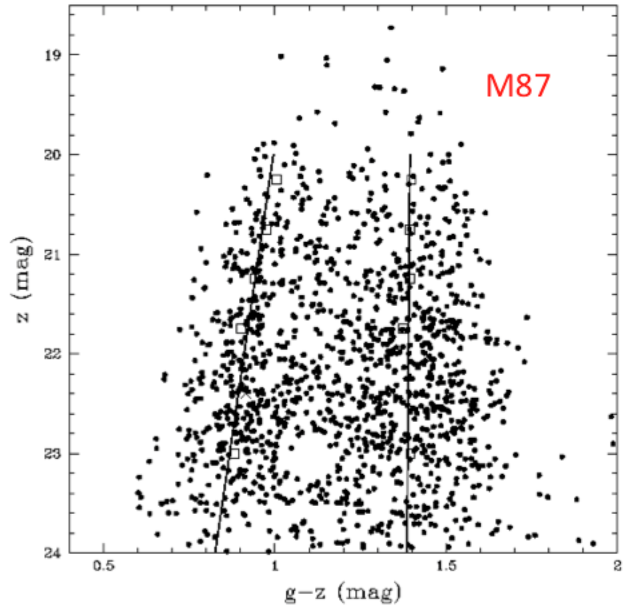

Figure 1.3: Color-Magnitude Diagram for M87. The MMR is visible at the most massive, most luminous metal-poor clusters. Strader et al. (2006)

1.1 summarizes a few MMRs previously found in elliptical galaxies.

Much of the work on elliptical galaxies and the MMR has been done in the Virgo and Fornax galaxy clusters. The Virgo cluster (VC) is at the center of the Local Super Cluster and contains the nearest collection of gEs. The nearby Fornax galaxy cluster (FC) also contains a handful of gEs ideal to study the MMR. Peng et al. (2006) Peng et al. (2006) conducted a comprehensive photometric study of a hundred early-type galaxies in the VC. Most galaxies in the survey had luminosities of -22 $<M_v<$-15 and showed the expected color bimodality for massive galaxies. To convert their (g-z) HST/ACS filters to metallicity they used the following conversion,

$$[Fe/H] = -2.75 + (1.83 \pm 0.23)(g - z) \tag{1.1}$$

for the blue part of the range. Most of the biggest, most luminous galaxies studied by Peng et al. (2006) showed a MMR. Mieske et al. (2010) Mieske et al. (2010), carried out a similar study in both the VC and the FC. The latter found a mass-

Galaxy ID	*MMR slope* (α)	*Reference*
NGC 3115	0.100 $\pm$ 0.07	Jennings et al. (2014)
NGC 1407	0.413	Harris (2009)
NGC 3348	0.663	Harris (2009)
NGC 3258	0.614	Harris (2009)
NGC 3268	0.128	Cockcroft et al. (2009)
NGC 4696	0.517	Cockcroft et al. (2009)
NGC 4278	0.55 $\pm$ 0.10	Usher et al. (2013)
NGC 1399	0.82	Mieske et al. (2010)
NGC 4649	0.28	Faifer et al. (2006)
NGC 5557	0.049	Cockcroft et al. (2009)
NGC 5193	0.31	Cockcroft et al. (2009)
NGC 3311	0.71	Cockcroft et al. (2009)
IC 4329	0.32	Cockcroft et al. (2009)
M87	0.48	Strader et al. (2006)
M49	none	Strader et al. (2006)

Table 1.1: Summary of Observed MMRs in Elliptical Galaxies. Uncertainties added when available/possible.

metallicity relation for the merged data of both clusters of Z $\sim M^{0.43\pm0.12}$. Their data set was divided in four different subsamples, low-mass, high-mass, FC galaxies and VC galaxies. CMD of the low- and high-mass samples and a description of the changes in slope between the VC and FC can be seen in figure 1.4. To convert their colors to metallicity they referred to Peng et al. (2006), see equation 1.1.

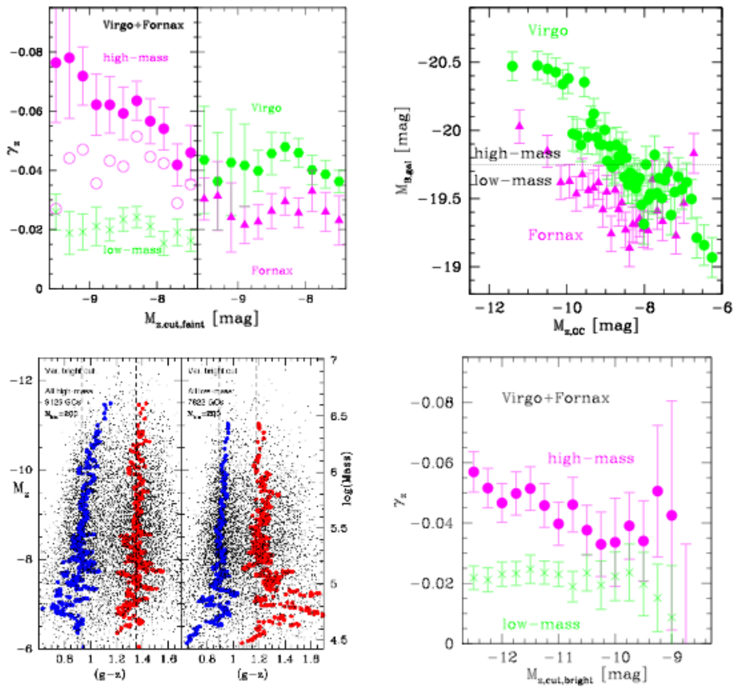

Figure 1.4: Upper left: Variation in the MMR slope as a function of the magnitude cutoff for the Virgo and Fornax sample. Upper right: Variation in the MMR slope as a function of the magnitude cutoff for the Virgo sample. Bottom left: CMD diagram for the high- and low-mass sample. Bottom right: MMR slopes as a function of the bright magnitude cutoff (Mieske et al. (2006)).

Figure 1.4 serves as a confirmation that the most massive and luminous GCSs will exhibit a MMR, but as one goes below a certain magnitude cut-off the metal-poor sub-population has a small slope. The upper left panel also shows that the slope becomes steeper as the GCS reaches the highest masses. From these results, the VC seems to have a more prominent MMR than FC which could have to do with the fact that the VC is significantly more massive than the FC. With the exception of one giant elliptical M49, or NGC 4472, all other gE showed a MMR in the VC. The lack of a MMR in M49 had already been observed by Strader et al. (2006).

The MMR in Spiral Galaxies

Statistically speaking, the largest GCS populations belong to ellipticals and, in principle, the best locations to clearly measure the MMR. However, the MMR has been observed in spiral galaxies. Table 1.2 summarizes the previously published literature on the MMR of spiral galaxies.

Galaxy ID	*MMR slope* (α)	*Reference*
M 104	0.3	Harris et al. (2010)
NGC 5170	0.42	Forbes et al. (2010)

Table 1.2: Summary of Observed MMRs in Spiral Galaxies. Uncertainties added when available/possible.

The Sombrero galaxy, M104 contrary to most spirals, has a significant globular population; it is the disk galaxy with the largest GCS. This galaxy is fairly close to the MW and its disk lies in our line of sight avoiding any reddening effects. Hence, it is an ideal scenario to look for a MMR slope. Using wide-field HST data, W. E. Harris et al. (2010), found two clearly divided color peaks in the CMD diagrams. The (B-R) colors showed that the blue, metal-poor sequence became progressively more metal-rich towards higher luminosities while the red-sequence remained vertical over the full luminosity range. The MMR measured had Z $\sim M^{0.3}$, which is similar to what has been found in elliptical galaxies.

While smaller than M104, NGC 5170 also exhibits a MMR. Forbes et al. (2010) used the B and I filters on board of the HST Advanced Camera for Surveys to study the GCS of NGC 5170 (Forbes et al. (2010)). The CMDs reveal two subpopulations, a metal-poor and a metal-rich, with the metal-poor becoming redder as the subpopulation becomes more massive. The latter has the form of Z $\sim M^{0.42}$.

The existence or non-existence of the MMR in spiral galaxies is a source of confusion. The previous examples suggest that both early- and late type galaxies exhibit a MMR. The reason for the lack of a MMR in the MW is not directly related to the morphology of the galaxy, but with the size of its GCS. The statistics in a sample that small will not provide an appropriate description of the MMR. The MW harbors around 100 clusters while NGC 5170 and M104 harbor over 600 GCs.

The Enigma of the Massive Elliptical Galaxy, M49

M49, or NGC 4472, is the most luminous galaxy in the Virgo Cluster with a magnitude of M_v = -22.6, see figure 1.5. M49 lies about four degrees from the center occupied by the massive elliptical M87. M49 also possesses an outstanding bimodality with two distinct metal-poor and metal-rich subpopulations (Geisler, Lee, and Kim (1996)).

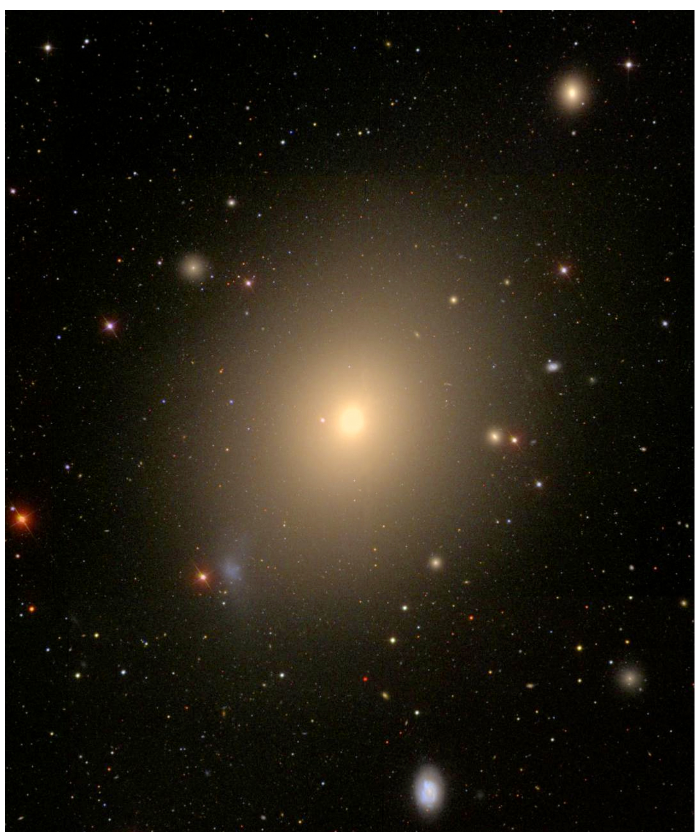

Figure 1.5: M49. Credits: NASA

Given that M49 is a massive luminous elliptical with a populous GCS it is only natural to expect a well defined MMR slope in its color-bimodality. But, M49 does not appear to show any signs of a MMR slope. Strader et al. (2006) and Mieske et al. (2006) both report a firm non-detection in M49. Figure 1.6 from Mieske et al. (2006) shows the CMD diagram for three different elliptical galaxies in the FC and the VC, respectively. The right-most plot shows the CMD for NGC 1399 and the slope in color in its metal-poor population is clear. M87 (left-most plot) follows a similar path to NGC 1399, whereas the metal-poor subpopulation in M49 is firmly straight at the highest masses.

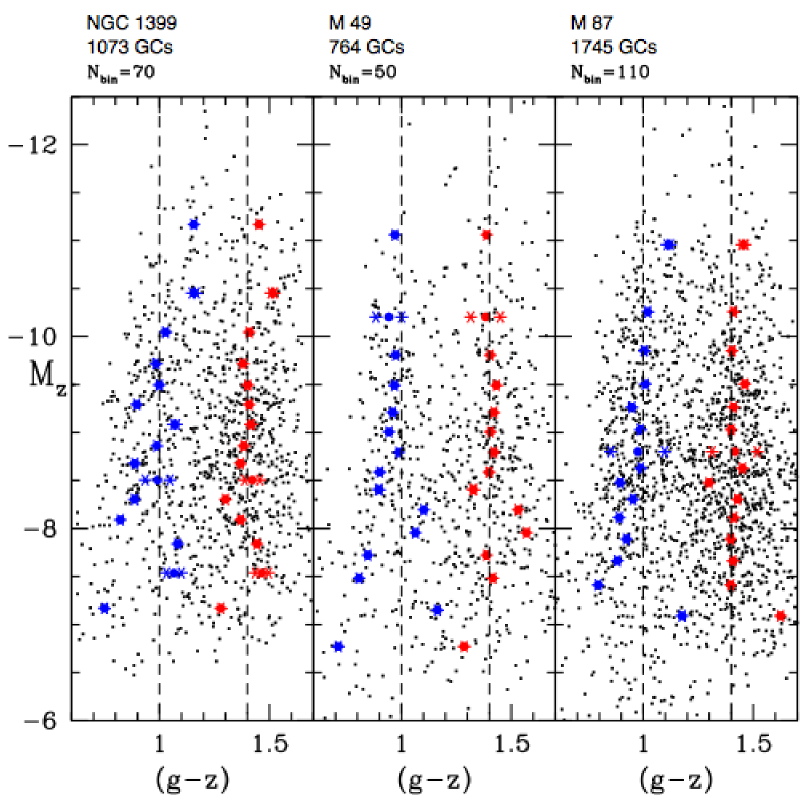

Figure 1.6: CMDs for three massive elliptical galaxies, NGC 1399, M49 and M87. Mieske et al. (2006). Blue and red stars shows the best-line fit.

NGC 1399 is the giant elliptical located at the center of the FC with a luminosity

M_v = -21.74 (Faber et al. (1989)) and with a population of globular cluster of roughly 6,500 (Faber et al. (1989); Forbes, Grillmair, Williger, Elson, and Brodie (1998)). Similarly, M87 is a massive elliptical galaxy located at the center of the Virgo cluster; only slightly less luminous than M49, and with a very rich GCS. Hence, there are no major superficial differences between the three galaxies. This lack of a MMR slope in M49, could be due to the fact that M49 is not a central galaxy unlike NGC 1399 or M87. However, the MMR has also been detected in non-central galaxies like IC4329 or NGC 5170. It is unknown how many other gEs besides M49 do not have a MMR, but the implications of massive galaxies not showing a MMR are important. It is likely that the MMR is directly related to the individual history and formation of each galaxy.

1.5 Mechanisms of the MMR

In this section, the discussion will point to possible mechanisms that could potentially explain the MMR in massive galaxies.

1.5.1 Merged Star Clusters

Mieske et al. (2006) and Strader et al. (2006) suggested that the "blue tilt" could be a result of merged star clusters. This idea was quickly disregarded since the majority of the objects in the metal-poor subpopulation are small compared to the size expected from merged GCs. The Large Magellanic Cloud is an example of a galaxy with a handful of clusters, such as NGC 1846, massive enough to be the result of mergers. However, the number of merged clusters needed to create to the MMR is too high; therefore, mergers could account for part of the MMR, but they cannot be the main driving mechanism of the MMR (W. E. Harris et al. (2006), Strader et al. (2006)) .

1.5.2 Gravitational Capture of Metal-Rich Field Stars

Mieske and Baumgardt (2007) proposed the gravitational capture of metal-rich field stars as candidates to enrich the metal-poor subpopulation of the GCSs in gE. Bica, Dottori, Rodrigues de Oliveira Filho, Ortolani, and Barbuy (1997) suggested that star clusters of roughly $10^5 M_\odot$ orbiting 1kpc from the Galactic Bulge could have accreted a significant amount of matter throughout its lifetime. Field stars belonging to gE are substantially more metal-rich than the members of the metal-poor subpopulation of the GCSs. Hence, capturing such stars could potentially enrich the metal-poor population of clusters. The red, metal-rich subpopulation of clusters would not see a significant change since its metallicity is similar to that of the field stars. However, using N-body simulations, Mieske and Baumgardt (2007) recreated the scenario for a typical, high mass, luminous globular cluster similar to what it is seen in the 'blue tilted' metal-poor population of clusters and concluded that this process is far too inefficient to account for the MMR.

1.5.3 Self-Enrichment

First suggested by Strader and Smith (2008) and Bailin and Harris (2009), the basic premise of self-enrichment is that CGSs start out by having a inital metallicity dictated by their birth-cloud; nevertheless, that protocloud can undergo internal self-enrichment throughout its evolution by supernovae (SNe). For self-enrichment to have significant effect, emphasis should be put in the most massive stars. High mass stars are responsible for most of the metal ejection in the globular cluster. This abundance of heavy elements is produced mostly inside SNe with progenitor masses of 20 $M_\odot$ or greater. The evolutionary timescale of massive stars is short. Hirschi (2007) calculated lifetimes of 6-10 Myr for $20M_\odot$ - $40M_\odot$. Recchi and Danziger (2005) found that most metals are released within the first 5 Myr after the first 100 star die and the timescale for the supernova ejecta to cool is similar, 7 Myr (McKee and Ostriker (1977)). Hence, even though stars with masses as low as $8M_\odot$ could explode as SNe, the timescale for self-enrichment is much shorter than the lifetime of such stars.

Bailin and Harris (2009), conducted a series of Monte Carlo simulations to determine whether the metal content in GCs comes solely from self-enrichment or if pre-enrichment plays an important role. Quantitatively, the Bailin & Harris self-enrichment model follows this behavior,

$$f_z = \frac{exp(-E_{SN} f_* r_t)}{10^2 M_\odot G M_c}, \tag{1.2}$$

where f_z is the fraction of total metals contributed by supernovae as a function of the progenitor star massand retained by the cloud, E_{SN} is the SNe release energy of $\sim 10^{51}$ erg, f_* is the star formation efficiency, r_t is the tidal radius and M_c is the mass of the cloud. The results from this model predict that the mass of the cloud plays an important role in the evolution of the MMR. The bigger the formed cluster, the better its retention of SNe ejecta. The simulations showed that the MMR should be expected for GCs with masses of 10^6 or greater. Their model also suggests that the main free parameter controlling the level and amplitude of the MMR is the star formation efficiency f_*. Interestingly, this model predicts the possibility of a red-tilt; however, if a MMR in the red population exists it would not be easy to observe since the addition of a handful of metals would not have the same effect on a population that is already metal-rich.

If self-enrichment is the main and only mechanism responsible for the MMR, this implies that the MMR slope should not vary significantly from galaxy to galaxy. A small MMR would be possible in this model if either f_* is very large (assuming a 100% efficiency) or if r_t is very large. However, the measured sizes of globular clusters are very similar in different galaxies and in brightest cluster galaxies (W. E. Harris (2009)). While it is an attractive model, recent data points otherwise; hence, another mechanism, perhaps, in unison with self-enrichment must be responsible for the

MMR.

1.5.4 Mass Accretion during Orbit Transit

Another mechanism that could potentially explain the MMR phenomenon is a mass accretion mechanism as the proto-cluster orbits the dwarf galaxy in which it formed. Bekki, Campbell, Lattanzio, and Norris (2007) investigated the abundance inhomogenity in GCs. They suggested that GCs forming in low-mass dwarf galaxies are polluted by gas ejected from AGB stars; hence, changing the metal abundance of the cluster. Maxwell, Wadsley, Couchman, and Sills (2014a) proposed a new framework for the formation of multiple populations in GCs. This theory assumes that all GCs that exhibit abundance spreads formed near the center of a high-redshift dwarf-sized galaxy progenitor. These objects then took part in the hierarchical build-up of present-day massive galaxies. As their gas cools down, it collapses and becomes dense enough to form molecular clouds and ignite star formation. The continuity of such events will then enrich the central "pristine" gas which will expand and trigger star formation. AGB stars are possible polluters of this event (Ventura & D'Antona 2005, D'Ercole et al. 2010). The outer shells of AGB stars produce Na, N, O and C which in high amounts could alter the metallicity of the young cluster. As the GC orbits the dwarf galaxy in which it formed, the GC will accrete gas and star formation will continue. Eventually, the GC will move to larger orbits where it can more easily escape from the dwarf galaxy. Each globular cluster can make multiple passages through the gas-rich center. Hence, this mechanism could potentially enrich the GCs with a cocktail of abundances within a few Myr of its formation. For SNe gas to be retained, the cluster needs to be massive, as stated by the self-enrichment model. The size of the cluster is not as crucial as for that of the self-enrichment scenario and SNe are not the sole polluters enriching the GCs. Also, each globular cluster will have a unique accretion history since each orbit will be different and the amount of gas in each orbit will also be different, making this process highly randomized. The latter would help explain why some galaxies show a MMR and why some do not. Hence, this scenario is highly dependent on the available gas of the galaxy which in turn is related to the galaxy's own dynamical history. It is not clear yet if the abundances of C, N, O and Na are sufficient to account for the MMR or if SNe along with AGB yields combined are the necessary ingredients for the MMR.

1.6 Aim of this Thesis

Summarizing the ground covered so far, GCs were thought to be simple systems composed of stars with identical chemistry and formation epochs. Yet, with the aid of new deep space-imaging and high-resolution spectroscopy, it has been shown that GCs harbor multiple stellar populations. An aftermath of the discovery of bimodality in GCSs was a possible relation between the color and luminosity of the GCSs. The relationship suggests that the more luminous or the more massive the GCs are, they appear to become redder (metal-rich). This phenomenon is known as the MMR or as the 'blue tilt'. The latter has been mostly observed in massive early type galaxies, although a few Milky Way-like spirals have exhibited a MMR. The existence of the MMR suggests that an internal or an external, or a combination of both, mechanism is occurring and causing the bluest clusters to become redder as they become more massive. There have been several mechanisms proposed to explain the origin of the MMR such as the pollution by stripped nuclei or field stars, self-enrichment and mass accretion during orbit transit.

This thesis intends to explore the interesting case of M49, a massive galaxy that appears to have the criteria to show a MMR slope in its metal-poor subpopulation. It will address the issue of the mechanisms responsible for producing the MMR, specially the self-enrichment and the mass accretion during orbit scenarios. Chapter 2 discusses the data acquisition and reduction techniques. Chapter 3 shows results of the data; Chapter 4 discusses the results, the mechanisms that could lead to the observed results and a comparison with previous works on M49 and the MMR mechanisms.

Chapter 2

Data Reduction

"Don't Panic."

- Douglas Adams, *The Hitchhikers Guide to the Galaxy*

2.1 Data

In order to do this science, we need lots of globular clusters. The raw images were obtained from the MOSAIC camera on the 4-m telescope in the CTIO at La Serena, Chile on the night of October 19, 2005. The MOSAIC wide-field camera has a field of view of 36' x 36' and pixel scale of 0.27"/pixel. Broadband imaging was done using the Washington filter (Geisler et al. (1996)), C and the Kron-Cousins filter, R. Even though, T1 is the traditional broadband Washington filter, the Kron-Cousins R filter has proven to be more efficient than its T1 counterpart. The Kron R filter has a larger bandwidth and a higher throughput than the T1 filter, yet their magnitudes remain similar with a small zero-point difference of 0.02 mag. An advantage of using the broadband Washington filters and the (C-T1) index for this analysis is their sensitivity to metallicity. Most of the literature on the MMR has been conducted in B, V, I, g', i', g, z, and the Washington filters are fairly easily converted to the latter. Figure 2.1 in page 31 shows the variety of the commonly used photometric filters and their respective wavelengths.

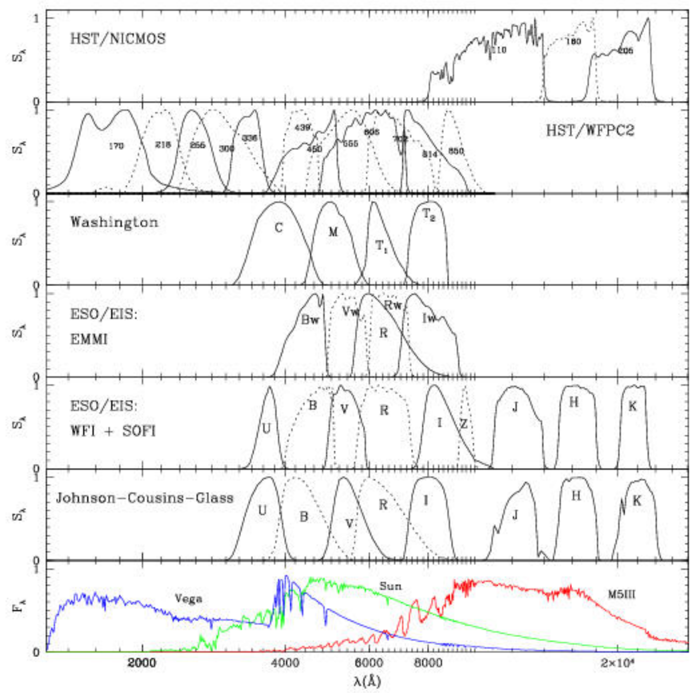

Figure 2.1: A collection of commonly used filters. Source: Padova Database of Stellar Evolutionary Tracks and Isochrones

2.2 Image Processing

The raw images were processed using several IRAF (Image Reduction and Analysis Facility) packages. To prepare the images for photometry we median-subtracted the isophotal background from M49 in order to allow the fainter objects to become more easily detected. To begin this process, the *imexam* IRAF task, a task that examines images, was used to measure the radial profile of several faint star-like objects in the image. Objects such as GCs will appear as star-like objects in these images. After an appropriate sky level was added to the raw images, the *imcombine* IRAF routine was performed in order to sum the list of images and get a single combined image in each filter. By appropriate background level, we refer to a constant sky level for the exposure time which is determined from the individual exposures. With these combined frames, we can start to determine which of the objects in the image are globular cluster candidates.

2.3 Object Detection and Photometry

2.3.1 Setting the Stage

To detect possible globular cluster candidates and carry out PSF photometry, the DAOPHOT IRAF package was used. Since GCSs in gE tend to be crowded environments, it is convenient to conduct PSF fitting photometry rather than aperture photometry given that the former is much more immune to crowded fields. DAOPHOT uses three main tables of parameters called *daopars*, *datapars* and *photpars*. The *daopars* table gives the numerical values of several quantities used in many places throughout the DAOPHOT subroutines needed to conduct the object selection and photometry. See below table 2.1 for summarized collection of most important parameters in a typical daophot table,

The FWHM of the images was determined from *imexam*, the PSF box size radius was set to 10 FWHM in order to fully see the shape of the outer-most wings of star-like objects. After several test runs, the detection threshold was set to 3σ above the sky average. The low cut-off bad pixel threshold was generously large, $\sim 10\sigma$ below the sky level. The fitting radius was set to a value roughly equal to the FWHM, the latter is small enough to avoid including foreign light, but large enough to measure most of the signal coming from the object. Parameters like the "gain keyword" and "readnoise keyword" were obtained directly from the image. The AN parameter refers to the analytical psf model which it defines numerically as a sum of an analytic function and its residuals. For our purposes, AN was set to auto; the software will pick the best fitting model (see next section). Finally, the VAR parameter determines whether the PSF is constant or changing across the frame,

Parameter	*Quick Definition*
FWHM	FWHM of PSF profile (pixels)
FIT	PSF fitting radius (pixels)
PSF	PSF box size (pixels)
READ	Read-noise in adu
GAIN	CCD gain (e- per adu)
TH	Detection threshold in sigma(sky) units
AN	Analytical PSF model of choice
LOWBAD	Low cut-off bad pixel threshold
HIBAD	High cut-off bad pixel threshold
VAR	Variable PSF Level

Table 2.1: Selected Daophot Parameters

e.g. linear variation in x and y or quadratic.

The *datapars* package's main task is to set the radii of the apertures to be used in the photometry routine. Finally, the *photpars* is the package that does the fit of the PSF with the parameters set within the previous tables to all stars in the frame simultaneously. There are other code parameters in addition to the ones mentioned above which can be changed as well; however, these are the crucial parameters to conduct PSF photometry.

2.3.2 PSF photometry and Globular Cluster Candidates

Obtaining a clean PSF is key in order to apply it to thousands of objects across the image field. We started by generating an objective and uniform catalog of star-like objects using the DAOPHOT subroutine, *daofind*. The key in finding the star-like objects with *daofind* lies in selecting a good threshold value. As mentioned in the previous section, a good starting point for this threshold is 3σ, where σ is the standard deviation of the sky. Making the threshold value too big will miss a significant amount of faint stars, yet setting a value that is too small will enhance false detections. With these parameters a total of 43,512 objects were found by *daofind*. We then ran a quick aperture photometry routine within the DAOPHOT package, *phot* subroutine. We only used one aperture ($\sim$ FWHM) instead of several since we do not intend to use aperture photometry, but we still need to set up the definition of the PSF and this is a fair initial guess at the magnitude of the objects found in the field by *daofind*.

To build the PSF, a handful of bright, isolated stars need to be selected in order for DAOPHOT to create a proper model. DAOPHOT tests several models and determines which one has the smaller error within the data. These models can be a combination of an analytical function such as a Gaussian or Moffat function which aids in modelling the core and the bright region of the star, a Lorentz function or a 'Penny' function which is a mix of a Lorentz and a Gaussian model. To select these stars, DAOPHOT uses a subroutine called *pstselect* which allows the user to inspect the profile of the desired number of stars to build the PSF from. The number of stars can be specified using the *maxnpsf* parameter in *pstselect*. There is no right number of stars; in theory, the more stars you have the better the PSF, granted that the objects selected are sufficently bright. After the candidates were selected, the DAOPHOT psf subroutine was used to construct the complete PSF model. While *pstselect* does a good job in selecting stars according to the parameters fed to the routine, we inspected each of them individually and in doing so, built a better PSF.

We first built the PSF using 50 bright, isolated star-like objects and setting the PSF to have linear variations in x and y, yet the resulting PSF subtracted image still had a significant amount of noise and a lot of faint residual stars. We re-calculated the PSF using 200 PSF candidate stars and a quadratic variation instead. Lastly, we ran the *allstar* routine to simultaneously fit the newly created PSF to the thousands of objects found using the DAOPHOT's routines. The resulting images, figure 2.2, are free of faint objects and other irregularities. The *allstar* routine outputs a file with several columns such as an assigned ID number, x coordinate, y coordinate, instrumental magnitude, error, local sky value, number of fitting iterations, chi, and sharpness. Of particular importance to this work is the chi and sharpness parameters which were used to discern between galaxies, false detections and star-like objects. The sharpness of an object is related to the intrinsic angular size without any contributions from the atmosphere. If the latter, is close to zero, this object belongs to a point-source category which are our targets of interest. Similarly, a chi-value larger than 2 usually belongs to a background galaxy and not a globular cluster, stellar-like object, see figure 2.3.

Objects lying in the upper right quadrant of the both the C and R images were not considered for further analysis and removed from the sample due to the unreliability of the data in that area of the image. Central data was replaced by the central data measured reported in Geisler (1996) et al. as the central regions in our data were oversaturated.

2.3.3 Data Calibration

To create a master list of globular cluster candidates we matched the objects found by *allstar* in both images using a Python script and found a total of 40,257 matches. To calibrate the instrumental magnitudes obtained from DAOPHOT, we used the measured standard stars reported by Geisler et al. (1996). The zero point magnitude, m_{zp}, can be calculated by finding an average value of the magnitude of a handful of standard stars. Firstly, we matched our objects with the objects reported by Geisler and obtained a magnitude average of the matched standard magnitudes. Then, we added the calculated zero-point to our instrumental magnitudes,

$$m = m_{zp} + m_{inst} \tag{2.1}$$

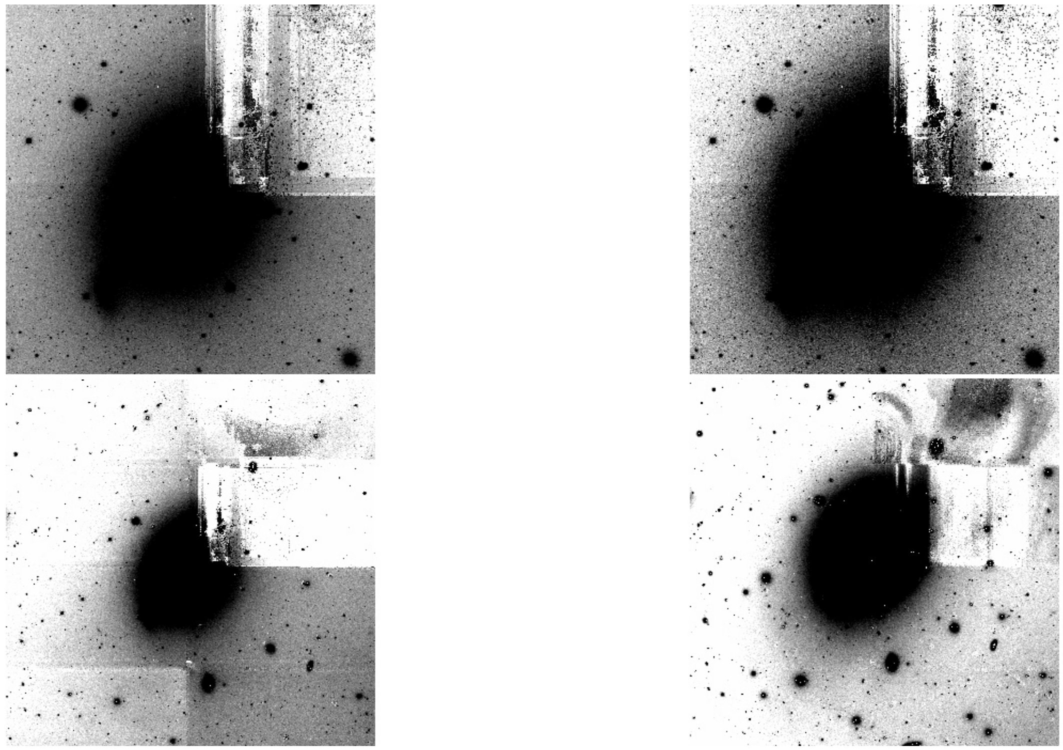

Figure 2.2: Top left and right: Raw C (blue filter) image and raw R (red filter) image. Bottom left and right: Cleaned, PSF fitted C (blue filter) and R (red filter) images. Faint square lines can be seen in the images coming from the shape of the CCD plates.

2.4 Color-Magnitude Diagrams

In order to visualize the MMR, we need to see how the magnitude changes with color in a Color-Magnitude Diagram (CMD). Recall that color is the difference between magnitudes for a given source in two different bands,

$$color_{ij} = m_i - m_j, \tag{2.2}$$

where i, j stand for C and R in this case. For the sake of discussion, it is worth noting again that these color measurements do not solely correlate with age. At this stage of the GCS evolution, all members are old. Metal-poor objects tend to appear

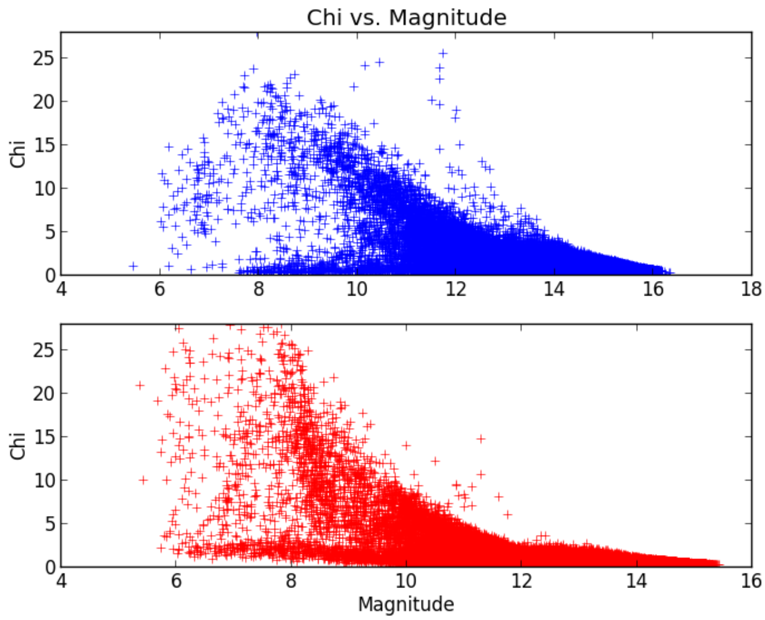

Figure 2.3: Top: Chi (*allstar* parameter) vs. Magnitude (C) Bottom: Chi (*allstar* parameter) vs. Magnitude (R). All objects lying above a chi of ~ 2 were removed.

bluer than metal-rich objects due to line blanketing by metals, particularly iron, in the atmospheres of stars or opacity not because of age.

Figure 2.4 shows the raw CMD. While many non-stellar objects were removed by *allstar*'s sharpness and chi parameters, many of the objects that appear in this CMD are not GC or members of the GCS. These objects might be the result of field stars or background contamination. Methods to clean the CMD of non-globular clusters are discussed below.

2.4.1 Radial Density Profile

In order to determine cluster membership, the field was divided in two equal areas and a dividing radius was computed as follows,

$$xy = 2\pi r^2. \tag{2.3}$$

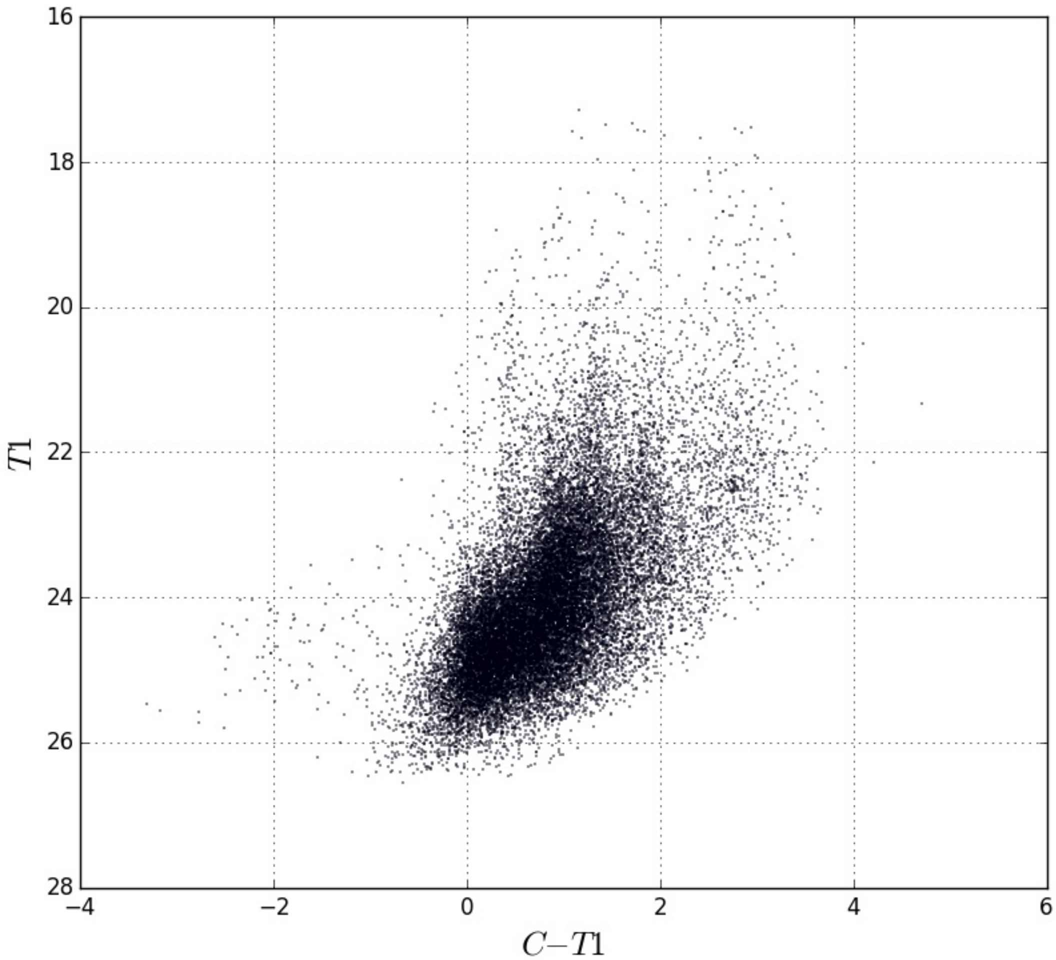

Figure 2.4: Uncleaned CMD for M49 using MOSAIC data with upper right quadrant removed. Each dot is a possible globular cluster; however, many of the detected objects are contamination from field stars.

Objects lying outside this radius are less likely to belong to the galaxy's GCS. One way of checking this radius is by counting the density of GCs as a function of the distance to the galactic center. To measure the cluster density, we divided the image in concentric circles of equal area centered at the galactic center, see figure 2.5. Then, using a python script, the number of GCs per circle was counted using the following equation,

$$GC/Area = \frac{\#_{clusters}}{\pi(r_{out}^2 - r_{in}^2)}, \tag{2.4}$$

and the error by using $error = \sqrt{\#_{clusters}}$. The cut-off for this background level was roughly at 10 arcmin^2 and can be see in figure 2.6, where the red line indicates where the cut was made.

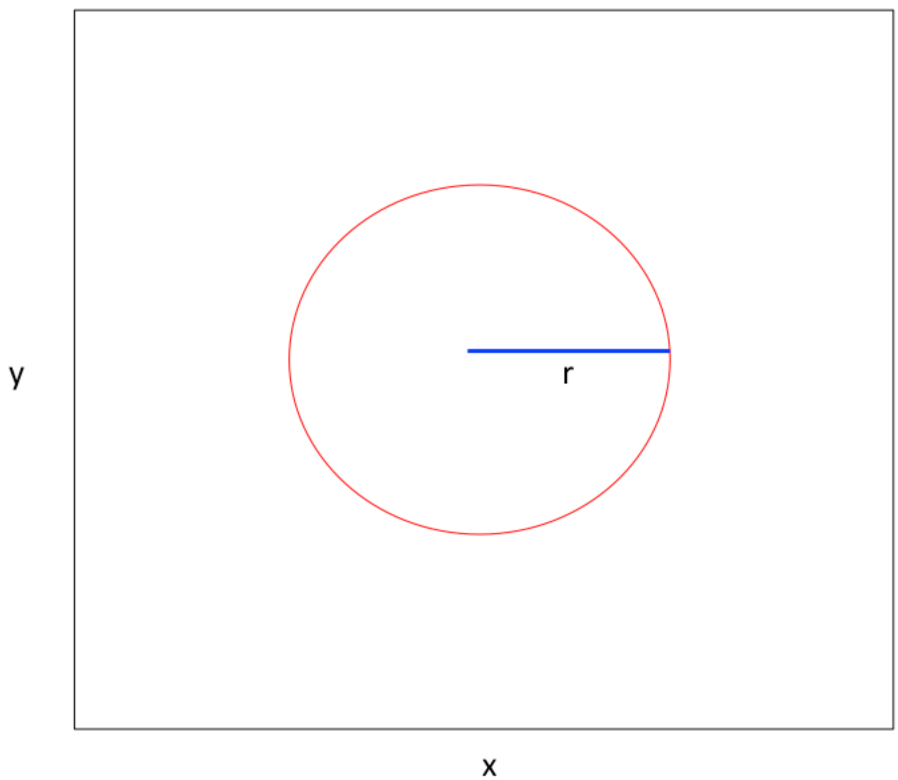

Figure 2.5: Schematic of the splitting of the image.

2.4.2 Statistical Cleaning and Magnitude Cut

In order to further clean the sample we conducted a statistical cleaning. The CMD in figure 2.4 was divided into two different areas of equal size which we will refer as inner and outer areas. Then, the CMDs for both areas were split into a grid of size

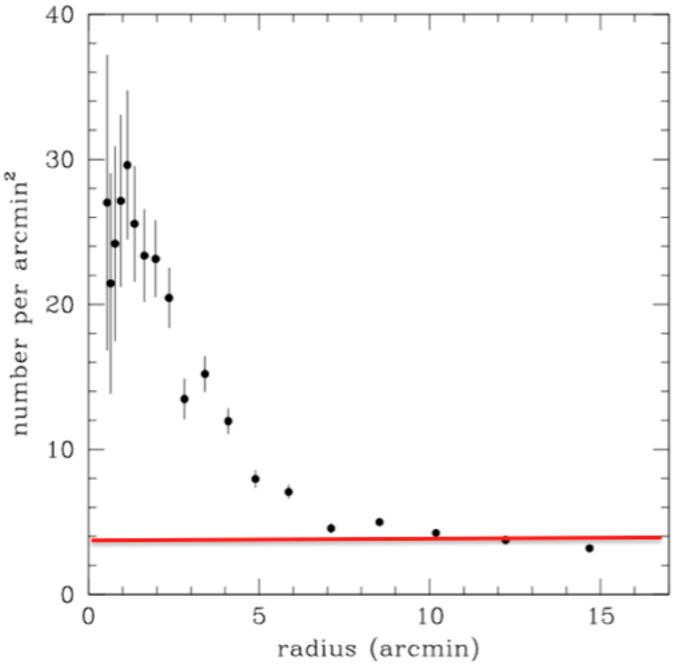

Figure 2.6: Background level cut-off for M49. Red line indicates the background level, objects beyond a radius of 10 arcmin^2.

of 0.2 in color by 0.4 in magnitude. All grids were compared to each other and if a match was found in the same box of the inner and outer areas then the object was removed from the sample, see diagram 2.7. By comparing the inner area in figure 2.8 to the outer area in figure 2.9, it is apparent that there are features that are present in 2.8, but not in 2.9 and it is those objects that we are interested in keeping.

The final CMD, 2.10 shows barely any false hits or field stars, but since we are interested in only the highest mass clusters, we made a final cut in magnitude of R $<$24.

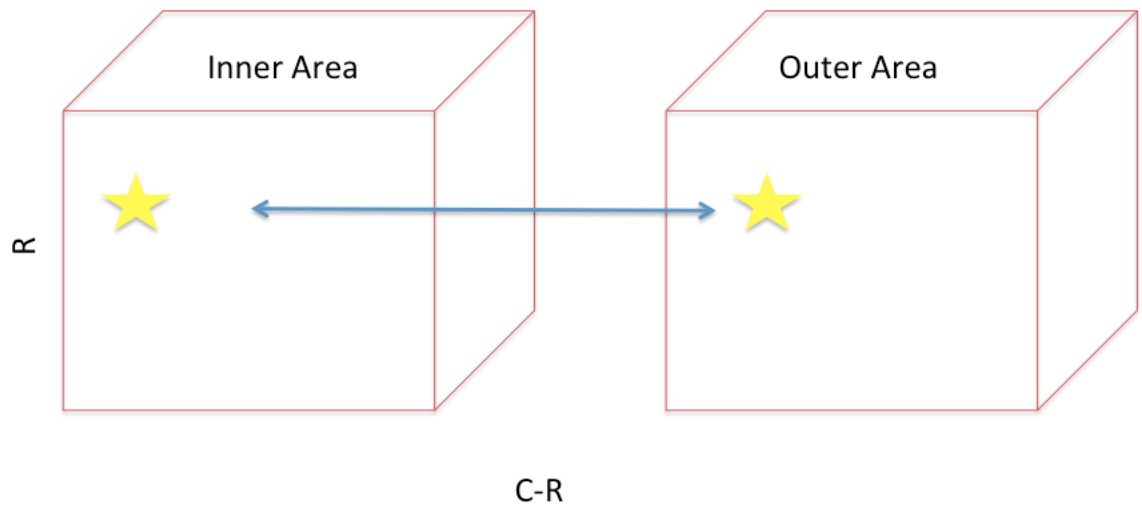

Figure 2.7: Statistical Cleaning Diagram. Statistical cleaning was done by dividing the sample in two areas of equal size. A box of grid of size of 0.2 in color by 0.4 in magnitude was used to determine whether the object would remain in the sample. If the object was found in both regions,it was removed from the sample.

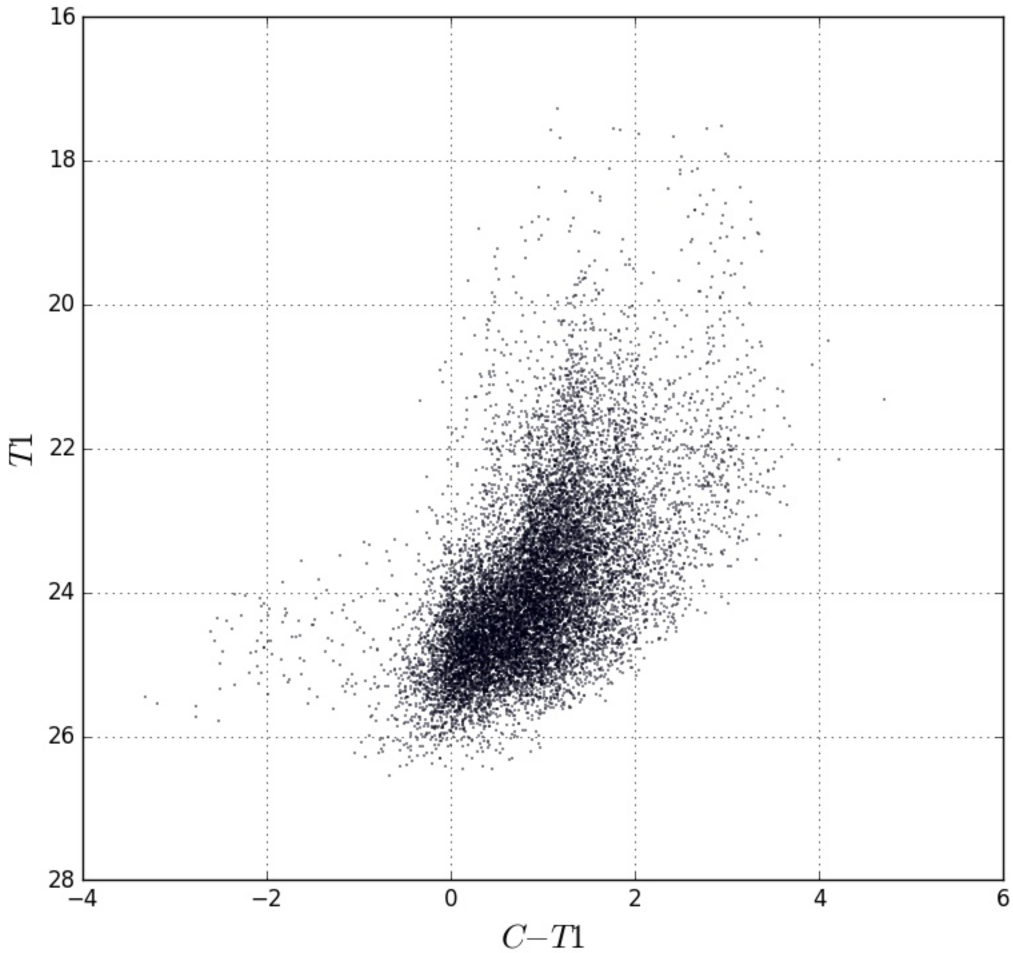

Figure 2.8: Inner area of CMD of M49. The full data sample was divided into two areas of equal size to statistically determine which objects are noise and/or field stars.

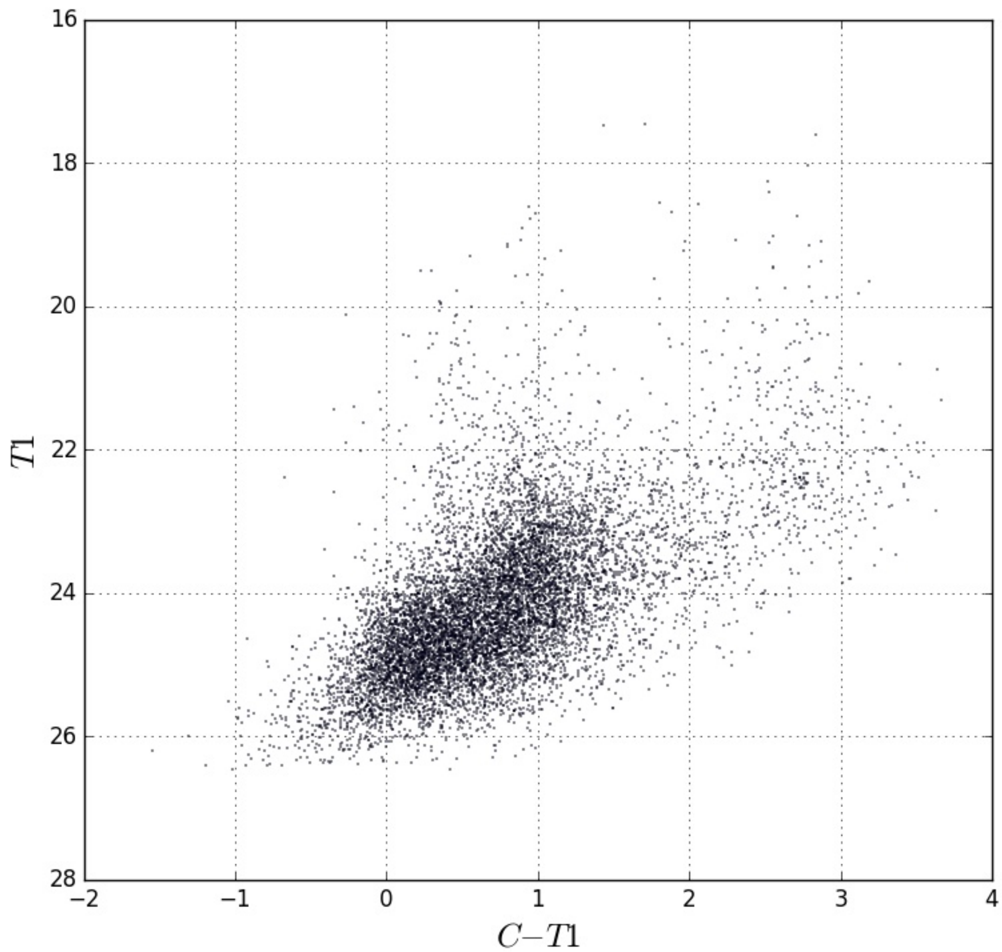

Figure 2.9: Outer area of CMD of M49. Outer area of equal size to the inner area; both areas will be compared to statistically remove unwanted objects.

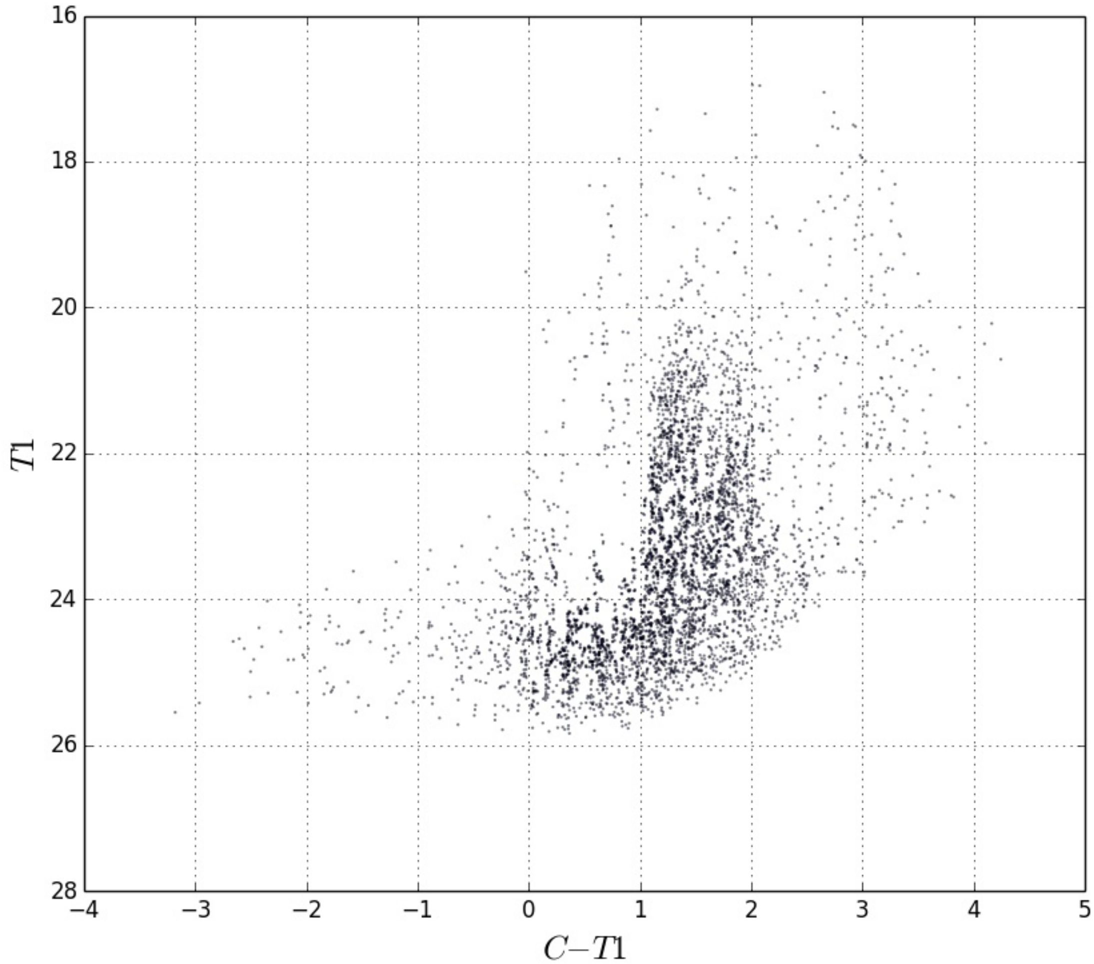

Figure 2.10: Cleaned, subtracted CMD of M49. Resulting sample after the inner and outer areas were matched and compared. The matching box was of 0.2 in color by 0.4 in magnitude. Matched objects were removed from the sample. The objects on the far right are M-stars; these stars have similar metallicities to the metal-ric GC population.

Chapter 3

Results

"We demand rigidly defined areas of doubt and uncertainty!"
- Douglas Adams, *The Hitchhiker's Guide to the Galaxy*

3.1 Analysis of the Color-Magnitude Diagrams

The first step in the analysis is to test the color distribution of the GCS for a clear presence of bimodality. The CMD diagram shown in image 2.10 in page 44 was grouped into color bins. The size of the bins was determined using the Freedman–Diaconis rule,

$$b = 2IQR(x)n^{-1/3}, \tag{3.1}$$

where b is the bin size (23 bins), IQR(x) is the inter-quartile range of the color data and n is the number of observations in the sample (2417 objects). The resulting histogram can be seen in figure 3.1 and two distinct populations are revealed. To quantitatively depict the observed bimodality and find the locations of mean color peaks, we used a GMM algorithm developed by Muratov and Gnedin (2010) which is a variant of the Ashman, Bird, and Zepf (1994) Gaussian mixture model, KMM. The

GMM algorithm will work on the premises that the distributions are Gaussian which in turn permits to test both homoscedastic (same finite variance) and heteroscedastic (different finite variances) distributions.

To determine the existence (or non-existence) of a color bimodality, the test must conclude that a bimodal fit significantly improves a unimodal fit. To do this, the GMM routine carries out an expectation-maximization (EM) test by comparing the likelihood ratio test of a sample having a unimodal distribution to a multimodal sample based on some initial user-defined guesses for the peak values and dispersions. The routine first determines the mean and the standard deviation with its respective uncertainties using one EM run and, subsequently, uses those values to build three statistics, (1) λ, the ratio of the maximum likelihoods, (2) D, the separation of the means relative to their widths and (3) *kurt*, kurtosis. The λ statistic behaves similarly to a χ^2 where, according to McLachlan 1987, the number of degrees of freedom are given by, excluding mixing proportions, twice the number of parameters contained within the two models in question. The D peak separation parameter used in this routine is very similar to the parameter used in Ashman et al. (1994) who stated that a *kurt* separation value of 2 or above is required to confidently describe individual peaks. Similarly, the *kurt* aids ruling out unimodality. A positive kurtois represents a sharp, single peak in the distribution while a zero or negative kurtois represents a flattened distribution. Hence, in the scenario of a sum of two populations, the kurtosis is expected to be considerably more negative.

These parameters on their own cannot rule out unimodality, however, the combination of the three provide a powerful tool in describing a possible multimodal population. Once these three statistics are computed, the routine will test if a unimodal description can be rejected in favor of a multimodal one and decide which scenario fits best among the following: (1) same variance, same mean, (2) different variance, same mean and (3) different variance, different mean. Finally, the routine runs a bootstrap to estimate the probabilities and errors of all the computed quantities.

Results from the GMM routine provided quantitative evidence that the distribution in figure 3.1 is bimodal with peaks located roughly at colors *(C-R)* = 1.32, σ = 0.31, N = 1718 objects (blue, metal-poor) and *(C-R)* = 1.88, σ = 0.29 and N = 698 objects (red, metal-rich). Out of the three scenarios depicted by the GMM routine, we used the different variances, different means scenario. The metal-poor fraction seems to be more populated than its metal-rich counterpart with 1718 and 698 clusters, respectively. To test if the GMM results were consistent with the more commonly used KMM routine from Ashman et al. (1994), we ran the color-binned sample with KMM to find the location of the peaks of the bimodal population. The main difference between both routines is that Ashman's mixture model assumes that the underlying population is described by the sum of two Gaussian modes and the probabilities are measured using a likelihood test, yet this test only behaves like a χ^2 if the populations have the same variances which is often not the case. The peaks obtained from the KMM routine were *(C-R)* = 1.36, σ = 0.20 (blue, metal-poor) and *(C-R)* = 1.81, σ = 0.21 (red, metal-rich). While the location of the peaks is not significantly different from the results obtained through the GMM, GMM values had a smaller dispersion value and showcased different statistical scenarios; hence, these values were used for the subsequent analysis.

3.2 The Mass-Metallicity Relation in M49

To find line fits to the blue and red populations and measure possible MMR slopes, we divided the data sample in two different sets by color. The dividing color was chosen to be the color where the blue and red population have the same number contribution, *(C-R)* = 1.56.

The linearity or non-linearity of the MMR is still not fully understood; however, inspection of the CMD showed in figure 2.10 reveals a curved pattern, rather than a linear relationship. We applied a quadratic polynomial regression to measure the strength of the slopes of both subsamples using the dividing color as the cut-off point to determine their slopes. The measured fits for the metal-poor and the metal-rich populations were,

$$(C - R) = -0.005R^2 + 0.159R + 0.197 \tag{3.2}$$

for the metal-poor subpopulation and,

$$(C - R) = -0.009R^2 + 0.421R - 2.922 \tag{3.3}$$

for the metal-rich subpopulation.

Because of the amount of scatter present in the data and the behavior of the MMR at the highest masses, a higher polynomial fit would best describe the underlying distribution of the data.

To test the strength of slope, we used the Spearman correlation coefficient which is a statistical measure of the strength of a monotonic relationship between paired data. We obtained correlation coefficient of -0.19 for the metal poor correlation which implies a weak monotonic relation between metallicity and the highest masses. This is not very surprising given the fact that the computed MMR slopes are significantly smaller than the MMR slopes computed for other galaxies in the literature (see table 1.1 in page 19.)

3.2.1 Magnitude Cuts

It is worth exploring if the lack of a MMR slope is partly due to the method through which we are splitting our sample. To remove doubts as to whether this is a potential source of discrepancy, we created samples of different size with respect to color. The color box used in the previous section was between 0.5 $<$(C-R) $<$2.5; it is a size large enough to catch most of objects we are interested, but also small enough to exclude possible outliers. To test whether the MMR would be visible by using a different sample size, we used a sample with a color box size of 1.1 $<$(C-R) $<$2.1 and 0.0

$<$(C-R) $<$3.0 The color-binned histograms and higher order polynomial fits can be seen in figure 3.4.

The computed correlations in the 1.1 $<$(C-R) $<$2.1 sample were,

$$(C - R) = 0.008R^2 - 0.388R + 5.708 \tag{3.4}$$

and

$$(C - R) = 0.005R^2 - 0.245R + 4.537. \tag{3.5}$$

The slopes for the sample of 0.0 $<$(C-R) $<$3.0 were,

$$(C - R) = -0.023R^2 + 0.979R - 8.707 \tag{3.6}$$

and

$$(C - R) = 0.004R^2 - 1.830R + 10.103. \tag{3.7}$$

There does not appear to be a significant MMR slope in either sample. The latter cut does seem to have a steeper inclination, but this could be attributed to the fact that this cut includes a larger portion of contamination. A similar conclusion is reached: the data are consistent with a zero MMR.

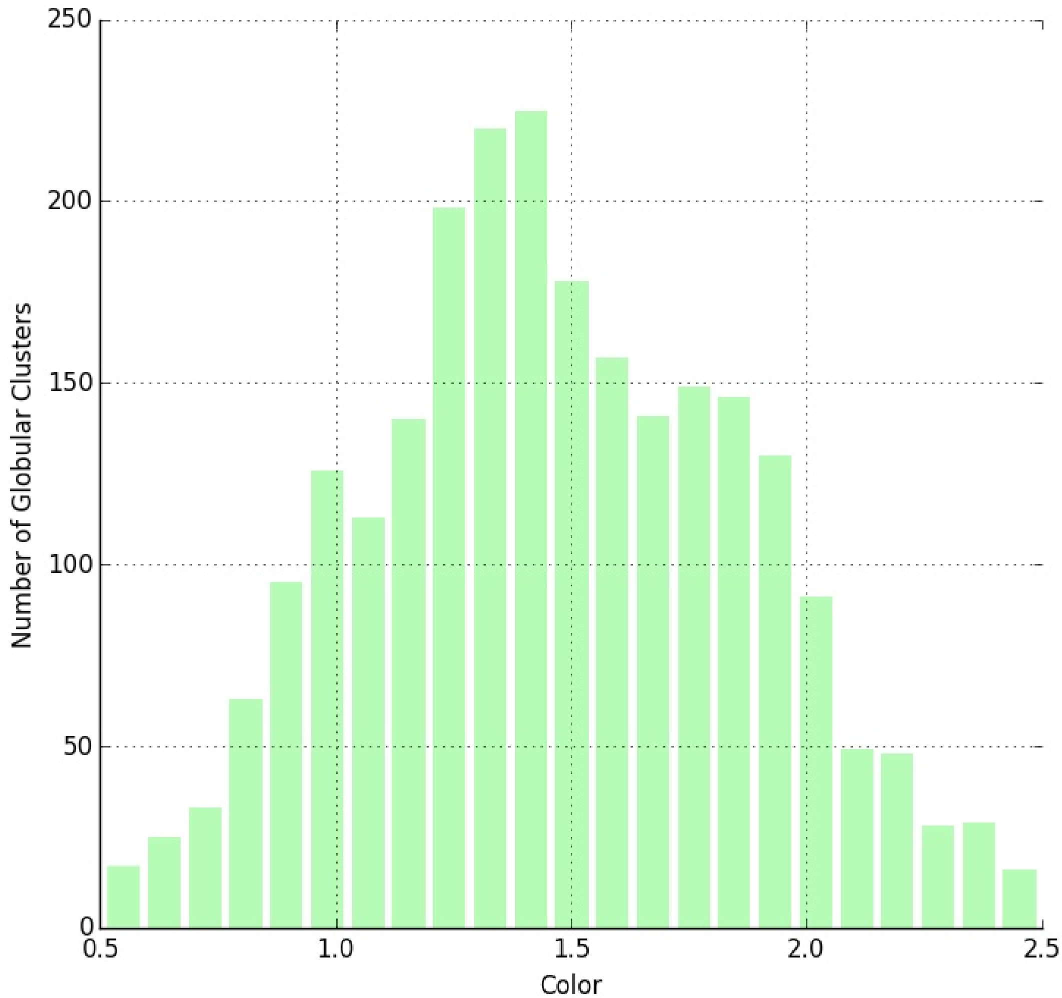

Figure 3.1: Color Binned Histogram of M49. Binning the sample in color bins allows for the bimodality to become easily observable, if present. The histogram shows two populations, with the blue peak being slightly higher than the red peak.

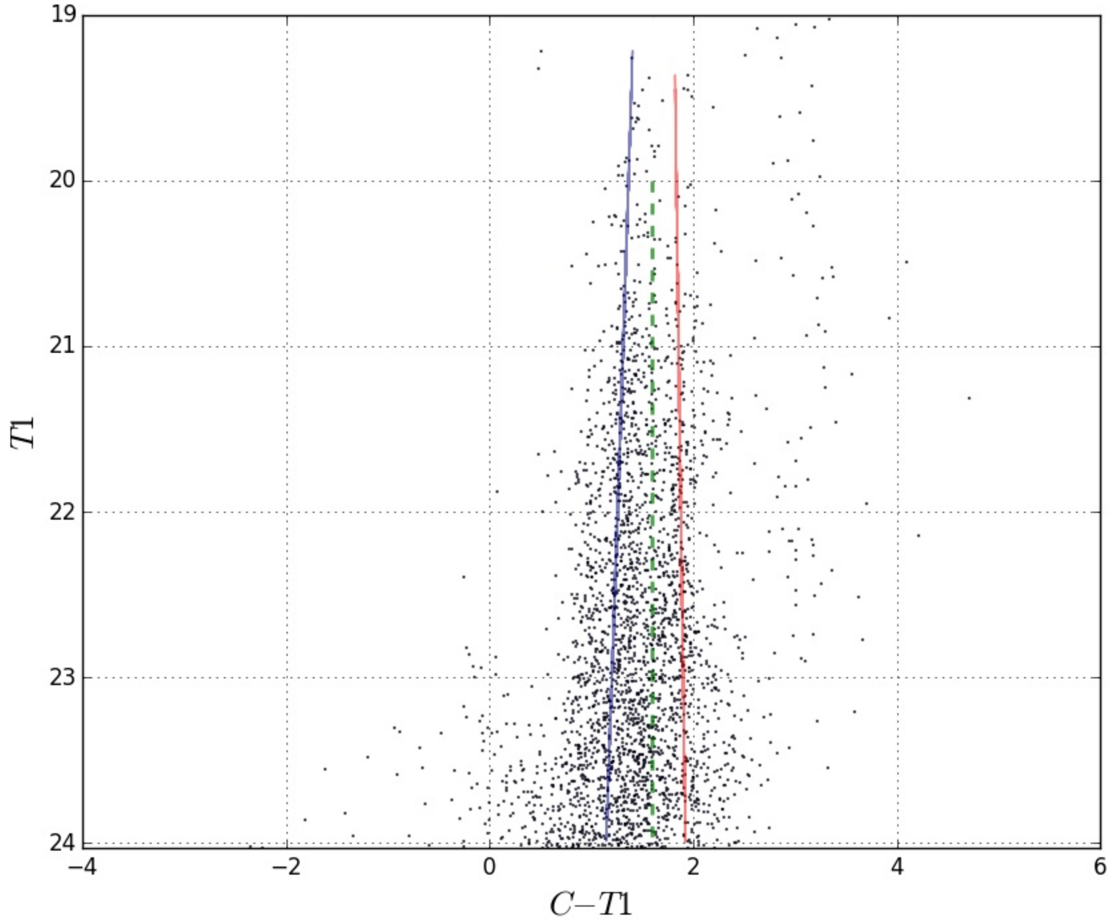

Figure 3.2: Higher Polynomial Fit to CMD of M49. A quadratic fit using a least squares regression was applied to the blue and red samples to obtain possible MMR slopes. The solid blue and red lines depict the quadratic least squares fit and the dashed green line represents the dividing color of the sample. The measured lines for the metal-poor and the metal-rich populations were (C-R) = -0.005R^2 + 0.159R + 0.197 and ((C-R) = -0.009R^2 + 0.421R - 2.922.

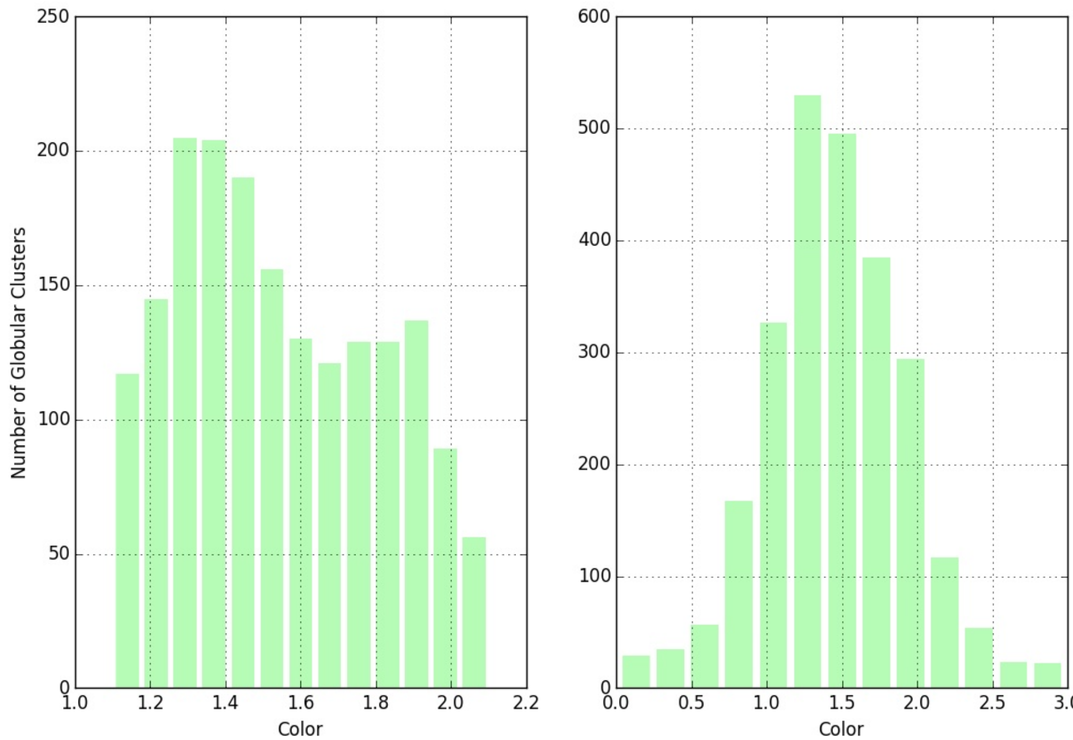

Figure 3.3: Left: 1.1 <(C-R) <2.1. Right: 0.0 <(C-R) <3.0. These histograms show that regardless of the arbitrary data cut-off, the GMM routine prefers a bimodal fit over a unimodal fit.

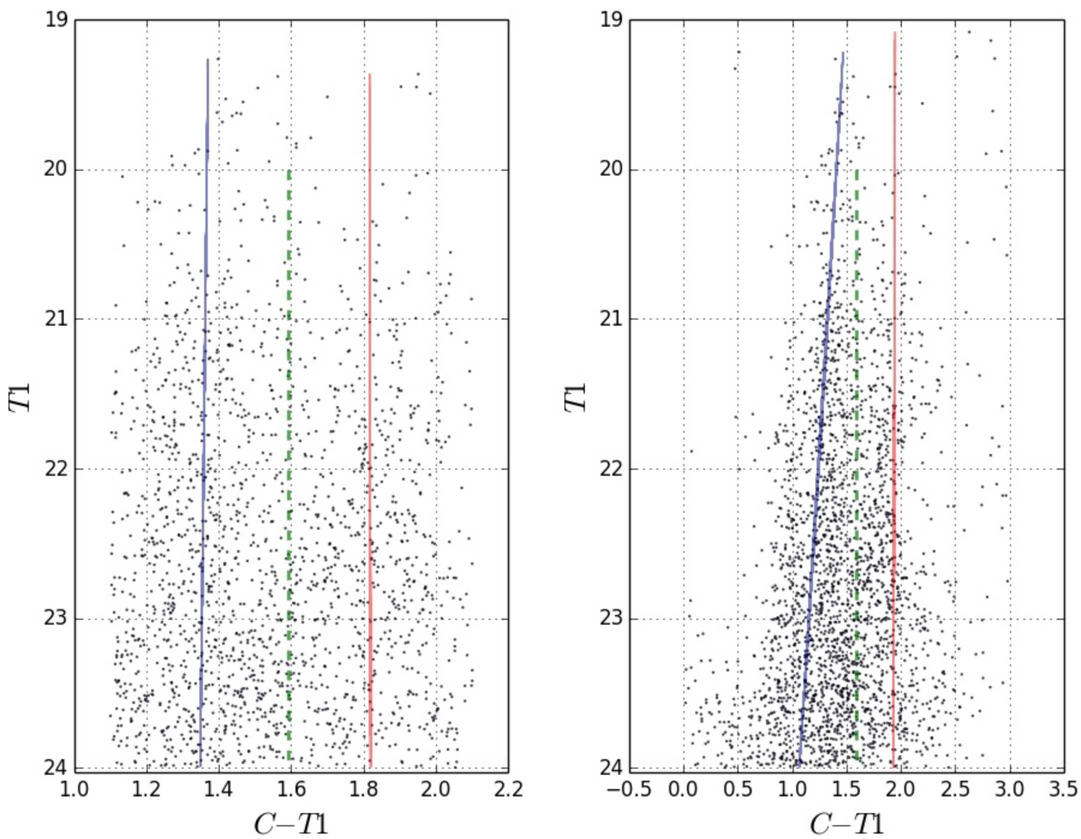

Figure 3.4: A quadratic fit using a least squares regression was applied to the blue and red samples to obtain possible MMR slopes. The solid blue and red lines depict the quadratic least squares fit and the dashed green line represents the dividing color of the sample. The measured correlations for the metal-poor and the metal-rich populations were $0.008R^2$ - $0.388R + 5.708$, $0.005R^2$ - $0.245R + 4.537$ (left) and -$0.023R^2 + 0.979R$ - 8.707, $0.004R^2$ - $1.830R + 10.103$ (right).

Chapter 4

Discussion

"Space is big. You just won't believe how vastly, hugely, mind-bogglingly big it is. I mean, you may think it's a long way down the road to the chemist's, but that's just peanuts to space."
- Douglas Adams, *The Hitchhiker's Guide to the Galaxy*

4.1 Analysis of the MMR in M49

4.1.1 Experimental Design: Metallicity Modeling

In order to test the theory suggested by Maxwell et al. (2014a), we recreated different scenarios of mass accretion and metallicity enrichment to determine the most likely scenario for M49. The key premise of the Maxwell et al. (2014a) approach is that all GCs with high abundance spreads formed near the center of the host dwarf galaxy and completed several orbits across a metal-rich center and in doing so accreted metals, enriching the cluster. They show that the orbits will become increasingly larger since the cluster will gain energy with each passage. Once the orbit becomes sufficiently large, the GC leaves the dwarf and accretion will be halted. The mass of the cluster should then start to diminish due to SNe feedback and subsequent stellar evolution. Assuming that AGB stars are the main polluters, these metal-rich winds,

$\sim$40km/s (Woitke (2006)) can be retained by globular clusters of roughly $10^4\ M_\odot$ to $10^6\ M_\odot$. SNe gas has speeds of roughly $\sim$500km/s and can escape the system with ease (typical escape velocities are in the order of $\sim$300km/s).

Since we cannot measure directly the parameters needed to simulate the observed metallicity changes, in the following setup, we treat the cluster mass, the metallicity and the accretion time as free parameters. To estimate the accreted mass rate we used the Bondi and Hoyle (1944) (BH) approximation as described by Maxwell et al. (2014a),

$$M_{rate} = 2\pi\alpha\frac{G^2M^2\rho}{({v_{rel}}^2 + c_s^2)^{3/2}}, \tag{4.1}$$

where M is the formation mass of the cluster, ρ is the surrounding gas density, c_s is the sound speed and v_{rel} is the relative velocity of the GC in gas cloud. According to Bondi and Hoyle (1944), the α value lies between 1 and 2, but we have chosen 1 for simplicity. We chose the initial formation mass of the GCs to be in the order of $10^{3-6}\ M_\odot$. The globular cluster mass cannot be less than the latter since it will not have the necessary potential to retain the AGB or Type II SNe ejecta (Bailin and Harris (2009)). Conroy and Spergel (2011) state that the GCs will spend a significant amount of time with relative velocities of 20-30km/s and assuming a cloud with a diameter of 300pc gives a time interval of about 10^7 years for the accretion processes in a single crossing. The sound speed was set to 10km/s for all the calculations (Maxwell et al. (2014a)).

In order to estimate the final metallicity as a result of multiple orbital crossings, we can setup the metallicity growth as follows,

$$Z_{final} = \frac{M_i z_i + M_{acc} z_c}{M_i + M_{acc}}, \tag{4.2}$$

where M_i is the formation mass of the cluster, M_{acc} is the accreted mass, z_i is the initial metallicity of cluster and z_c is the metallicity of the cloud. A good initial estimate of the primordial metallicity of the globular clusters from the blue and red subpopulations of M49 is their respective peak colors determined from the GMM routines, (C-T1) = 1.299 and (C-T1) = 1.884 To convert colors into metallicity we used the Harris & Harris (2002) conversion,

$$[Fe/H] = -6.037[1 - 0.82(C - T1) + 0.162(C - T1)^2]. \tag{4.3}$$

Using eq. 4.3 and taking into account proper reddening values (Canterna (1976)), the peak metallicities were -1.366 and -0.222 for the blue and red populations respectively. These values were used as the initial metallicity starting point for the simulation. The metallicity of the cloud was left as a free parameter in the simulation. With these initial assumptions of the system, we created metallicity tracks for the different masses. For a set of initial masses, an accreted mass was calculated; subsequently, with the array of accreted masses and a single cloud metallicity per iteration, an estimate of the final metallicity is computed. The cloud metallicities were changed after each iteration taking values from [Fe/H] = -3.0 to [Fe/H] = -0.3. Overall, our model has five adjustable parameters: time, velocity, density, initial mass and cloud metallicity. This simulation tracks the history of these globular clusters: from small mass clusters with low metallicity, to massive clusters becoming increasingly more metal rich. Each model runs for $\sim 10^6$ years. After each timestep the GC mass is recalculated (increases) and put back into equation 4.1. In a timestep of Δt, the mass increase is,

$$\Delta M = \Delta t \frac{2\pi\rho G^2 M(t)}{(v_{rel}^2 + c_s^2)^{3/2}} \tag{4.4}$$

, where *M(t)* is the GC mass at time *t*. Over many timesteps. the total accreted mass is then calculated. The resulting model tracks for both the blue and red populations can be seen in figures 4.1 and 4.2 respectively.

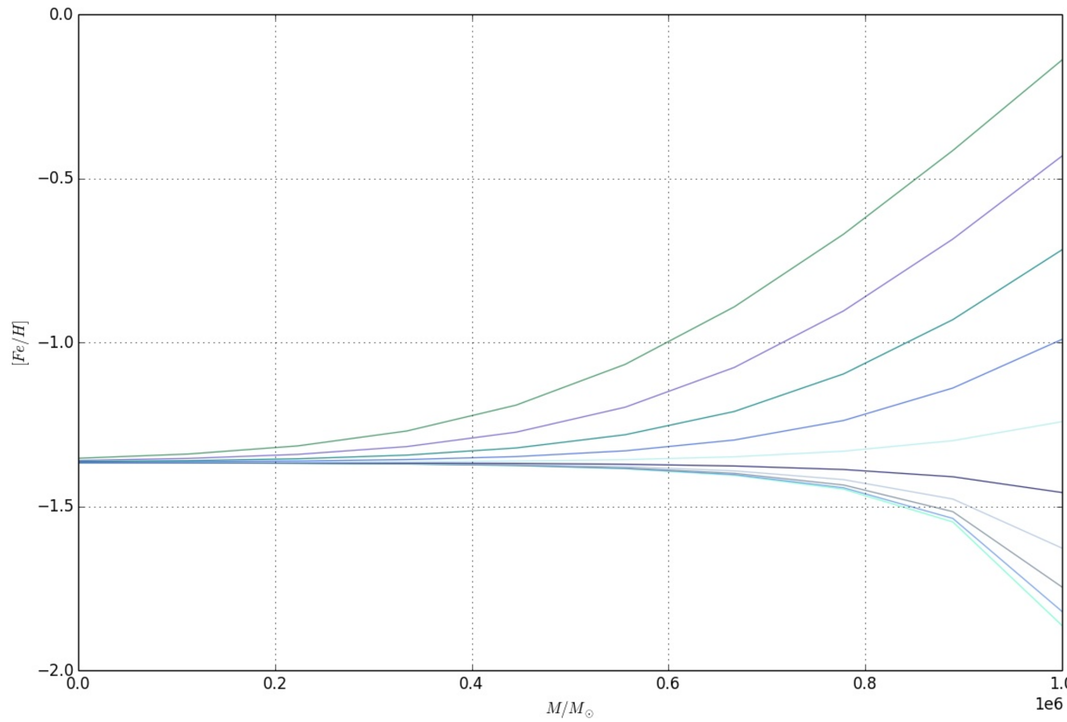

Figure 4.1: Mass Accretion Models for M49 (metal-poor population). Each line represents a different cloud metallicity running from -3.0 to -0.3. The metallicity is left as a free parameter. As the mass increases, and if the cloud is also metal-rich, the cluster itself will become more metal-rich. Detailed parameters are listed in table 4.1.

Each line in figures 4.1 and 4.2 belongs to the same array of initial masses, but different cloud metallicities. From the metal-poor model in figure 4.1, it appears that as the cluster becomes more massive and it passes a metal-rich cloud, it will result in a significantly more metal-rich cluster (top most line, dark green). The metal-rich model in figure 4.2 does not seem to follow the pattern of the metal-poor population. As predicted by the self-enrichment model, if there is any change in the metallicity of the metal-rich subpopulation, this change will be very small and not nearly as drastic as its metal-poor counterpart since this subpopulation is already metal-rich.

To explore the extent to which each parameter affects the metallicity distribution, we ran several combinations of the simulation. We started by using a smaller value for the velocity, 20km/s, and re-ran the simulation for the metal-poor population, see figure 4.3. A smaller velocity quickly reveals a higher final metallicity because the mass accretion rate is sensitive to v_{rel}, see top most teal line. A velocity of 25km/s reached a metallicity of -0.50 while a slower velocity of 20km/s reached metallicity values of -0.21.

Similarly, we ran the simulation for both the metal-poor and metal rich subpopulations with a smaller density, see figures 4.4 and 4.5. Table 4.1 summarizes the parameters used and approximate values.

Parameter	*Description*	*Value*
M_i	Initial mass of the globular cluster	10^3-$10^6 M_\odot$
z_i	Primordial metallicity	Peak metallicity of subpopulations
z_c	Added metals	-3 to -0.3 $[Fe/H]$
v_{rel}	Velocity with respect to gas	20-25km/s
t	Accretion Time	$\sim 10^6$ years
ρ	Density of cloud	1.0 x 10^{-19} - 3.0 x 10^{-19}g/cm3
r	Radius of cloud	200-300pc

Table 4.1: Range of Modelling Parameters

To compare the observed data and find the best-fit model in the simulation, we converted the calculated metallicities into color and, subsequently into apparent magnitudes. Distances to the Virgo cluster vary significantly, but we settled with 15.8 kpc (Puzia, Kissler-Patig, Brodie, and Huchra (1999)). To change from luminosity to magnitude a mass-luminosity relation of $M/L = 2$ was used (Webb et al. (2012), Webb et al. (2013)). The final mass of the cluster was multiplied by 1/2 to estimate the present-day cluster mass since the globular cluster will slowly lose mass throughout its evolution as shown by N-body modelling (Webb, Sills, and Harris (2013)), see diagram 4.6. Then, we overplotted the computed metallicity tracks over the observed data. Figures 4.7 and 4.8 shows the modelled metal-poor and metal-rich scenarios over the observed sample of M49. These line models portray how a family of clusters of different masses would evolve given an initial mass, initial metallicity and specific cloud conditions and velocities, see diagram 4.9.

Out of all the parameters used in this set up, it appears that the initial mass and the velocity of the system are the most influential parameters in obtaining a MMR slope. Velocity variations, see figures 4.1 and 4.3, seem to correlate with the initial mass of the cluster. Larger velocities require more mass, for a given cloud metallicity, to start changing the metallicity of the globular cluster.

4.1.2 M49

Previous studies (Mieske et al. (2010), Strader et al. (2006), etc.) have shown that M49 exhibits a clear bimodality in its globular cluster population, but does not seem show a MMR. Mieske et al. (2010) compared M49, the brightest galaxy in the Virgo cluster, to two massive ellipticals similar in morphology and luminosity to M49, NGC 1399 and M87, in order to put the scenario of M49 into perspective. According to W. E. Harris (2009), a large big GCS is needed in order to see any trace of a MMR. The latter explains why galaxies like the MW do not show a MMR. It could be argued that Strader et al. (2006) did not find a MMR in M49 due to their small sample size, 764 GCs, in comparison to the much larger sample sizes of NGC 1399 and M87 with 1073 and 1745 GCs, respectively. However, our analysis of a possible MMR in M49 adds similar results to previous literature. Our sample consisted of 2417 globular cluster candidates and while bimodality is present, there does not seem to be a relation between the bright end of the metal-poor subpopulation and the metallicity of said group. Mieske et al. suggests that a possibility for the lack of a MMR in M49 is due to the absence of a significant intermediate-color population of GCs; however, this gap between the metal-poor and the metal-rich population is observed in almost every MMR scenario (W. E. Harris (2009)). Hence, the lack of an intermediate population cannot be the deciding factor in the appearance of a MMR in the system. The fact that M49, a massive, bright elliptical galaxy with a significantly large globular cluster population does not show any evidence for MMR implies that there cannot be a unified model or process to explain the causes of this phenomenon.

The leading process attributed to the MMR is self-enrichment. Self-enrichment predicts that for the MMR to arise the GCS must have a significant number of globular clusters with masses of $10^6\ M_\odot$ or above. Many of the GCs in our sample belong in this category and, if the theory works as predicted, the MMR should be observable in M49. This leads us to speculate that there must be other factors in play in order to account for the variations we see from galaxy to galaxy. Several studies (Cen (2001); Bromm and Clarke (2002); Rhode et al. (2005); Brodie and Strader (2006b)) have pointed out that each galaxy's merging history may be crucial piece of the puzzle. Merging galaxies whose GCS have similar MMR relations would produce a galaxy with that same MMR slope; however, merging galaxies with different MMR slopes might not show a slope at all. Indeed, galaxies like M87 should have a more active and violent past than M49. M87 is located at the center of the Virgo cluster and central galaxies experience several dynamic interactions in their lifetime.

Part of the purpose of this study is to approach the MMR problem with a new perspective. Maxwell, Wadsley, Couchman, and Sills (2014b) suggest that the GCs will travel through the gas rich center of the galaxy and accrete mass and metals with each finished orbit. These orbits and, more importantly, the gas present in each orbit will be different; hence, the GCS metallicity may look different from galaxy to galaxy. The likely culprits of the gas enrichment are cocoon AGB stars whose outer gas layers can enrich the system with an overabundance of Na, N and O. Nevertheless, the Type II SNe gas feedback predicted by the Bailin and Harris (2009) self-enrichment model will have occurred much earlier than the orbital trajectory enrichment predicted by

Maxwell et al.; hence, it is still unclear how much influence these winds had on the resulting population. In the following sections, we discuss in greater detail the simulations obtained in the previous chapter using the orbital accretion approach.

4.1.3 Orbital Accretion

To examine the accretion and enrichment effects each globular cluster would go through in the trajectory to the dusty center of the galaxy, we followed the new framework proposed by Maxwell et al. (2014b) for forming multiple populations in dwarf galaxy globular clusters. We set up a multi-parameter model using the reasonable estimates for the system. The initial mass of the globular cluster was chosen to be in range of 10^3-10^6 $M_\odot$. GCs with masses 10^3-10^6 $M_\odot$ are not uncommon masses for these systems and MMR tells us that in order for any slope to be detectable, the GCs need to start out as massive entities. Below a certain mass or luminosity, (Bailin and Harris (2009)) estimate this mass to be in the order of 10^5-10^6 $M_\odot$), only the two subpopulations would be observed and no correlation between the mass and metallicity is observed. For the mass accreted by the globular cluster we followed the BH model for spherical accretion. Values for the rest of parameters involved in the analysis were listed in Table 4.1. Most of our parameters are free parameters and one could speculate about the arbitrariness or constraints of each; however, the ranges of values given to each parameter are not unreasonable. Using these ingredients, several model metallicity lines were computed using a Python-based script. From figure 4.7, it appears that a good fit model for the metal poor subpopulation is that of a cloud with a metallicity of [Fe/H] = -0.65 (olive track, fourth line from right), table 4.2 summarizes the best-fit parameters for the metal-poor subpopulation. The shape of metallicity lines confirm what was understood with regards to the behavior of the MMR, below a certain mass the metallicity lines will appear straight and gradually tilt as the system goes into higher masses. For the metal-rich subpopulation, the metallicity lines barely show significant change. Since the population starts out already metal-rich, adding a handful of metals will not change the metallicity in a striking manner. Hence, a MMR slope in the red subpopulation could potentially exist, but it would very hard to detect it. Indeed, there is a degree of degeneracy among the parameters of this model. For example, as can be seen in figures 4.1 through 4.4, smaller velocities have similar effects as larger masses.

Parameter	*Description*	*Value*
M_i	Initial mass of the globular cluster	10^3-$10^6 M_\odot$
z_i	Primordial metallicity	[Fe/H] = -1.366
z_{final}	Final abundance of GC	[Fe/H] = -0.65
v_{rel}	Velocity with respect to gas	25km/s
t	Time to cross cloud	$\sim 10^6$ years
ρ	Density of cloud	$\sim 1.2\text{x}10^{-18}$, radius = 300pc

Table 4.2: Best-Fit Modelling Parameters for M49

4.1.4 NGC 4696 vs. M49

Table 1.1 shows that many elliptical galaxies observed show a prominent MMR slope. M49, a giant elliptical galaxy, does not show an obvious MMR slope. The results shown in previous sections help explain the bigger picture of this phenomenon. A combination via SNe self-enrichment and a heavy-element abundance enrichment highly dependent on mass, initial metallicity of the cloud and velocity are capable of explaining the MMR. To test our model, we used *Hubble* B - I data of NGC 4696, a massive elliptical already known to show a prominent MMR slope (W. E. Harris (2009)). NGC 4696 is the brightest galaxy of the Centaurus cluster, located roughly 150Mly away and harbors several thousand clusters. Using a similar approach to M49, we determine the peak colors of NGC 4696 using the GMM routine. The blue and red peaks are located at (B - I) = 1.616 and (B - I) = 2.051 corresponding to metallicities of -1.45 and -0.29. Metallicity tracks are plotted over the data in figure

4.10 and figure 4.11. Table 4.3 summarizes the values obtained from the enrichment model for the best-fitting parameters of the metal-poor subpopulation. From figure 4.10, it appears that the purple track (third track from right) with a final metallicity of -0.43 fits the observed data well. More importantly, this shows that the orbit accretion model can explain both galaxies with an obvious MMR as well as galaxies without a MMR slope.

It is likely that the environment through which the GCS of M49 completed their formation was void of many metals whereas the contrary scenario was present within NGC 4696. As a BCG, NGC 4696 may have; therefore, begun star formation earlier and more rapidly, building up the average metallicity of the dwarfs in which GCs formed.

Parameter	*Description*	*Value*
M_i	Initial mass of the globular cluster	10^3-$10^7 M_\odot$
z_i	Primordial metallicity	[Fe/H] = -1.45
z_{final}	Final abundance of GC	[Fe/H] = -0.43
v_{rel}	Velocity with respect to gas	25km/s
t	Time to cross cloud	$\sim 10^6$ years
ρ	Density of cloud	$\sim 1.4\text{x}10^{-18}$, radius = 300pc

Table 4.3: Best-Fit Modelling Parameters for NGC 4696

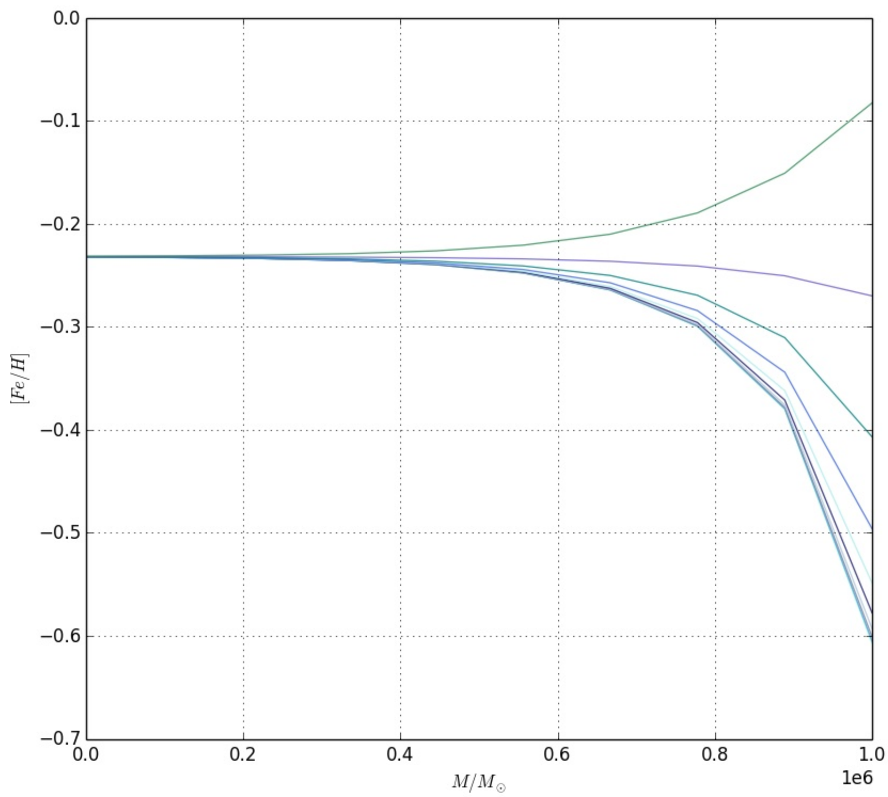

Figure 4.2: Mass Accretion Models for M49 (metal-rich population). Final GC metallicity is plotted versus the initial cluster mass. The metallicity is left as a free parameter. Contrary to the metal-poor subpopulation, there is not a significant change in the metallicity of the metal-rich population in either scenario. Metallicity decreases are due to accreting lower-metallicity gas. Detailed parameters are listed in table 4.1.

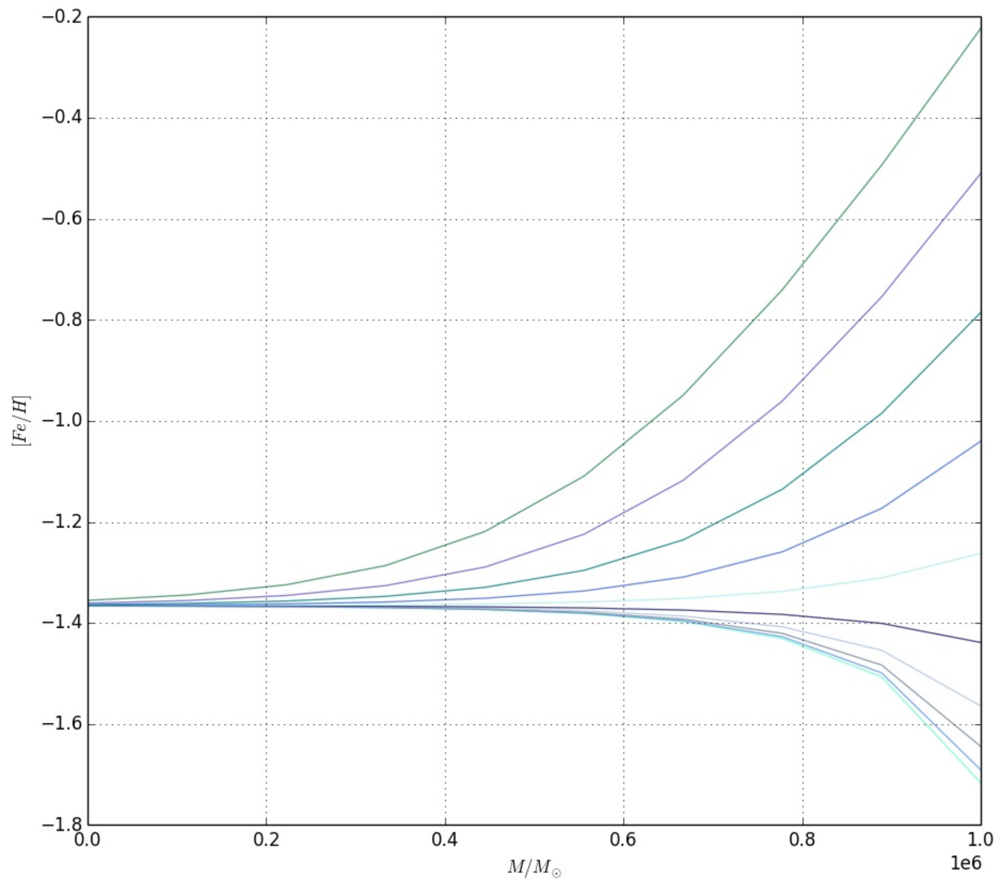

Figure 4.3: Mass Accretion Models for M49 (metal-poor population, smaller velocity). The velocity is decreased from 25km/s to 20km/s. A slower velocity allows the model to reach a higher final metallicity.

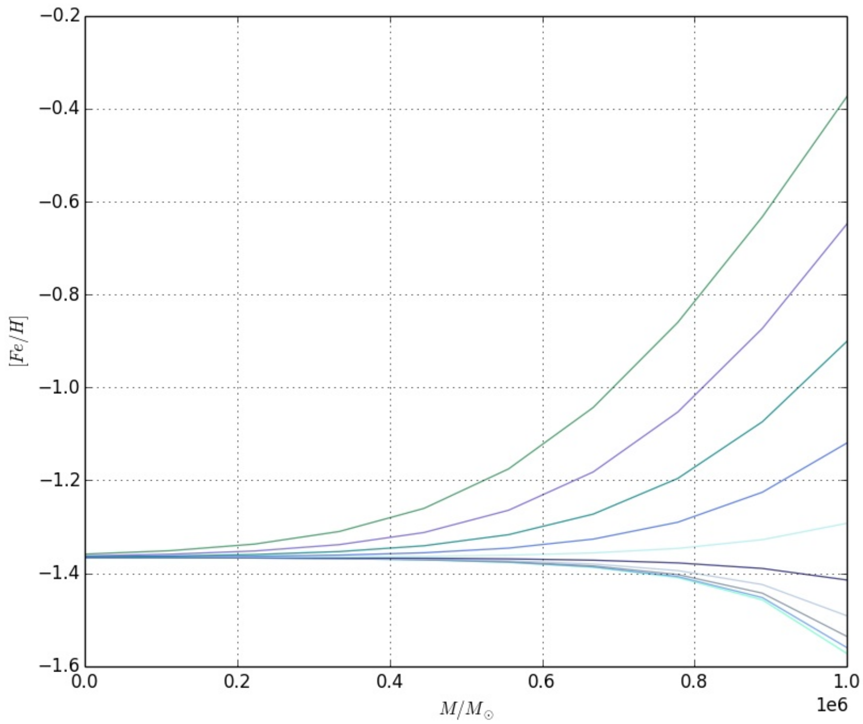

Figure 4.4: Mass Accretion Models for M49 (metal-poor population, smaller density). Similar to the smaller velocity scenario, a lower density environment will also produce and higher final metallicity.

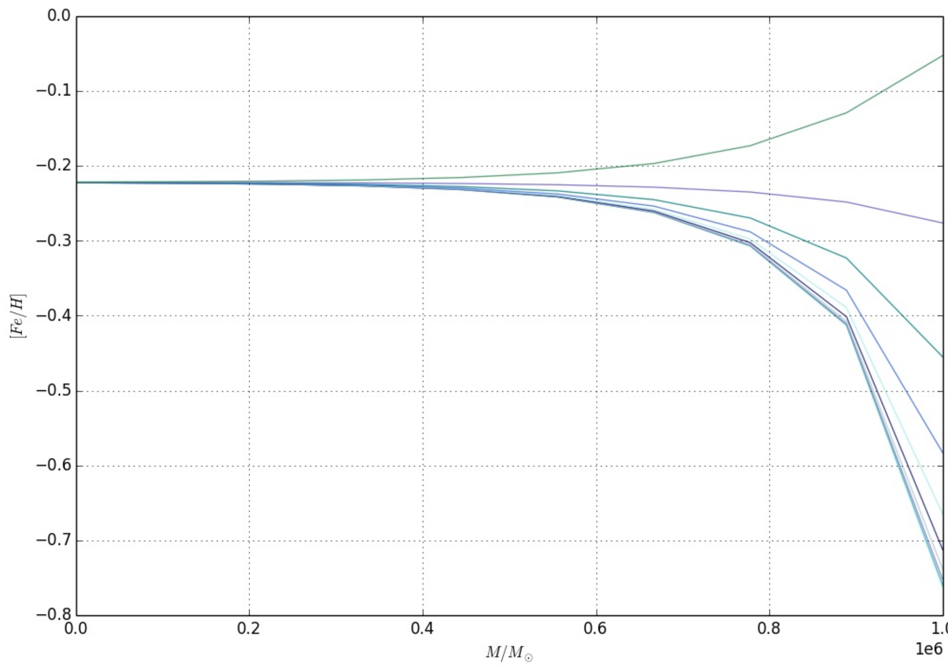

Figure 4.5: Mass Accretion Models for M49 (metal-rich population, smaller density). The final metallicity is slightly higher than that of the tracks on figure 4.2, but as predicted for a metal-rich subpopulation, changes will be small.

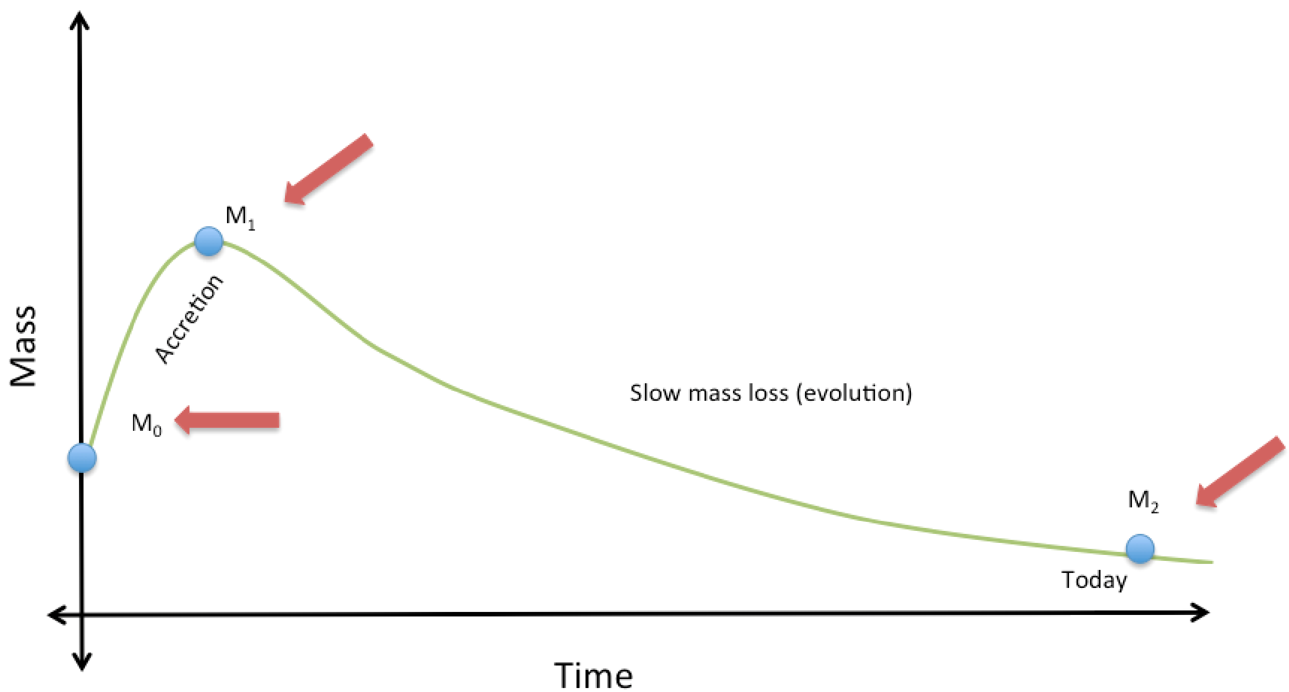

Figure 4.6: Final Mass in Metallicity Model. The GC will start with a mass M_o and once accretion starts it may gain almost twice its mass, yet this mass will slowly be lost once again due the GC's evolution.

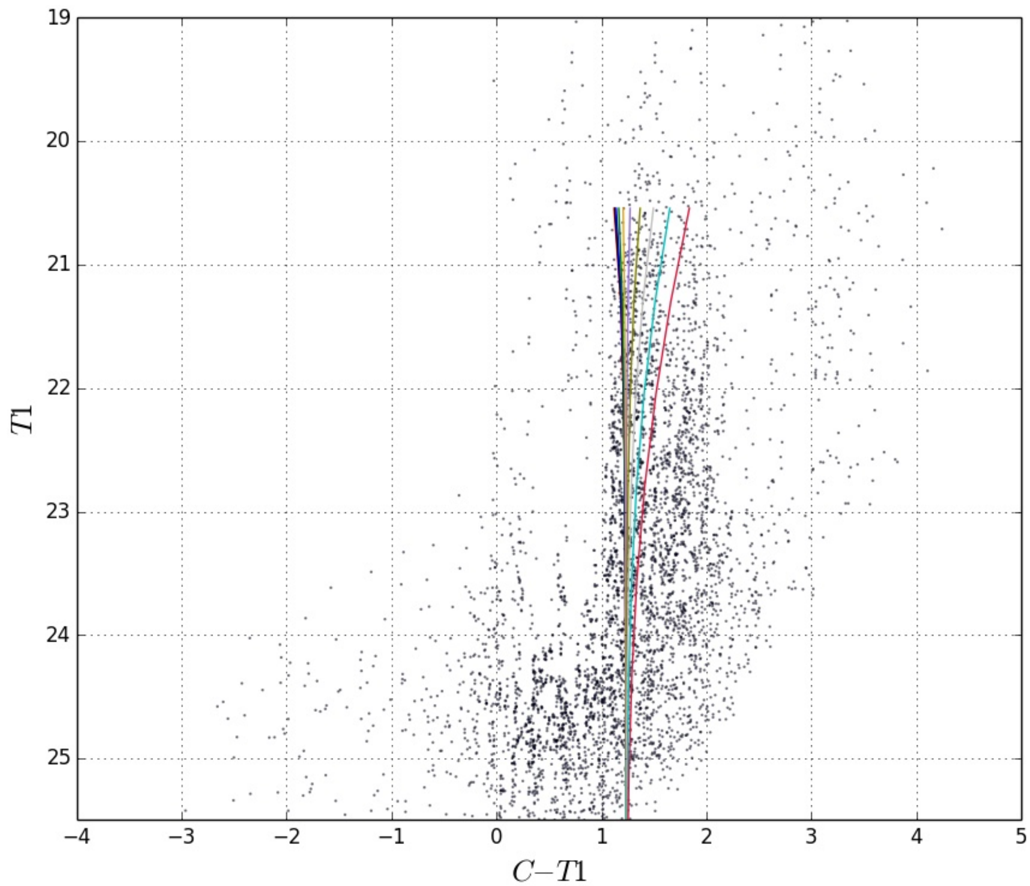

Figure 4.7: Metal-poor metallicity Tracks Over Data. Lines correspond to family of models seen in figure 4.3. The models in figure 4.3 were converted into metallicity using the final mass of the cluster and M/L = 2 luminosity relation. The dark olive line was the preferred fit with the lowest dispersion error.

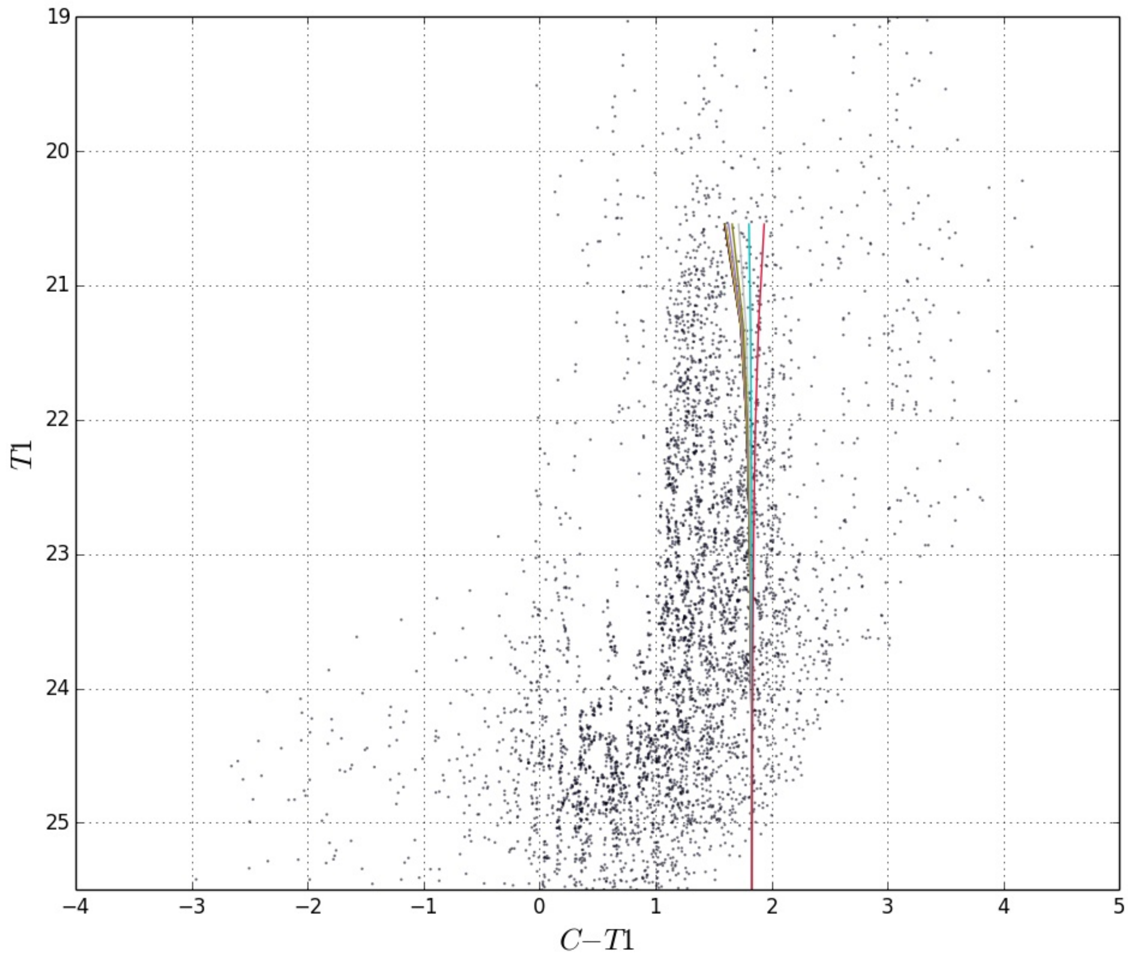

Figure 4.8: Accretion Models Over Data. Lines correspond to family of models seen in figure 4.3. The models in figure 4.2 were converted into metallicity using the final mass of the cluster and M/L = 2 luminosity relation.

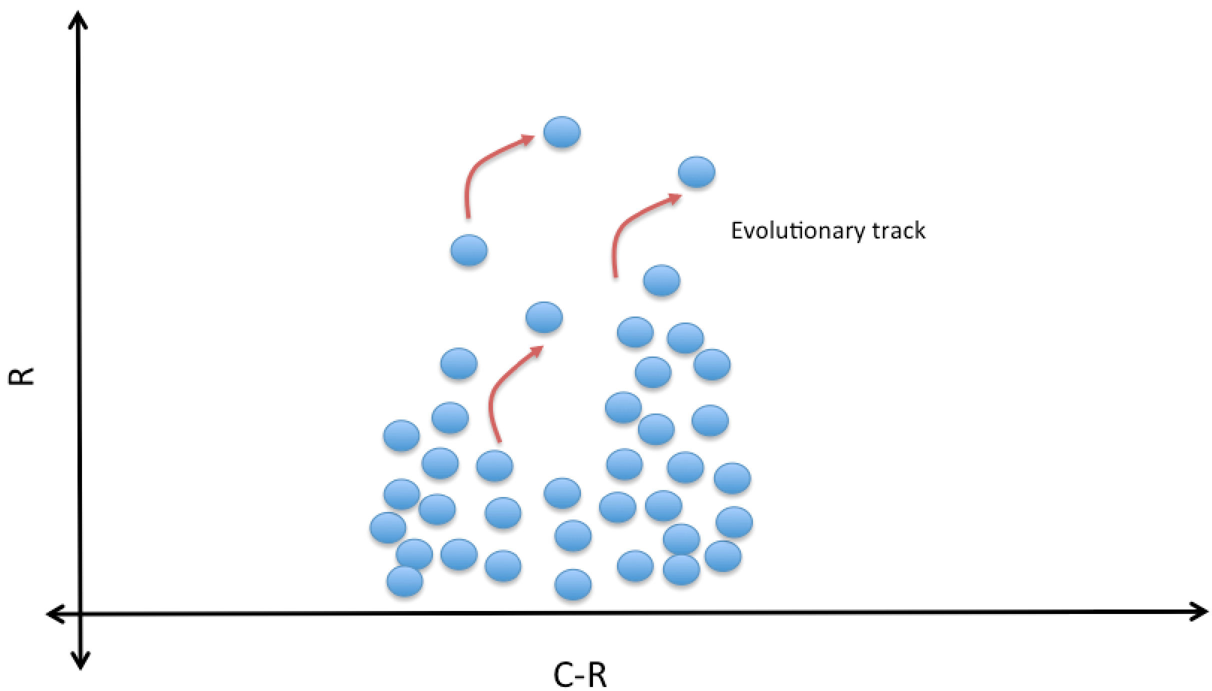

Figure 4.9: Metallicity Tracks Diagram. The lines shown in red are an example of a metallicity track connecting initial and final (at end of accretion) luminosity and color. For a given cluster with an initial mass and metallicity and that goes through a cloud of a specific heavy element abundance, gives the observed result in the data.

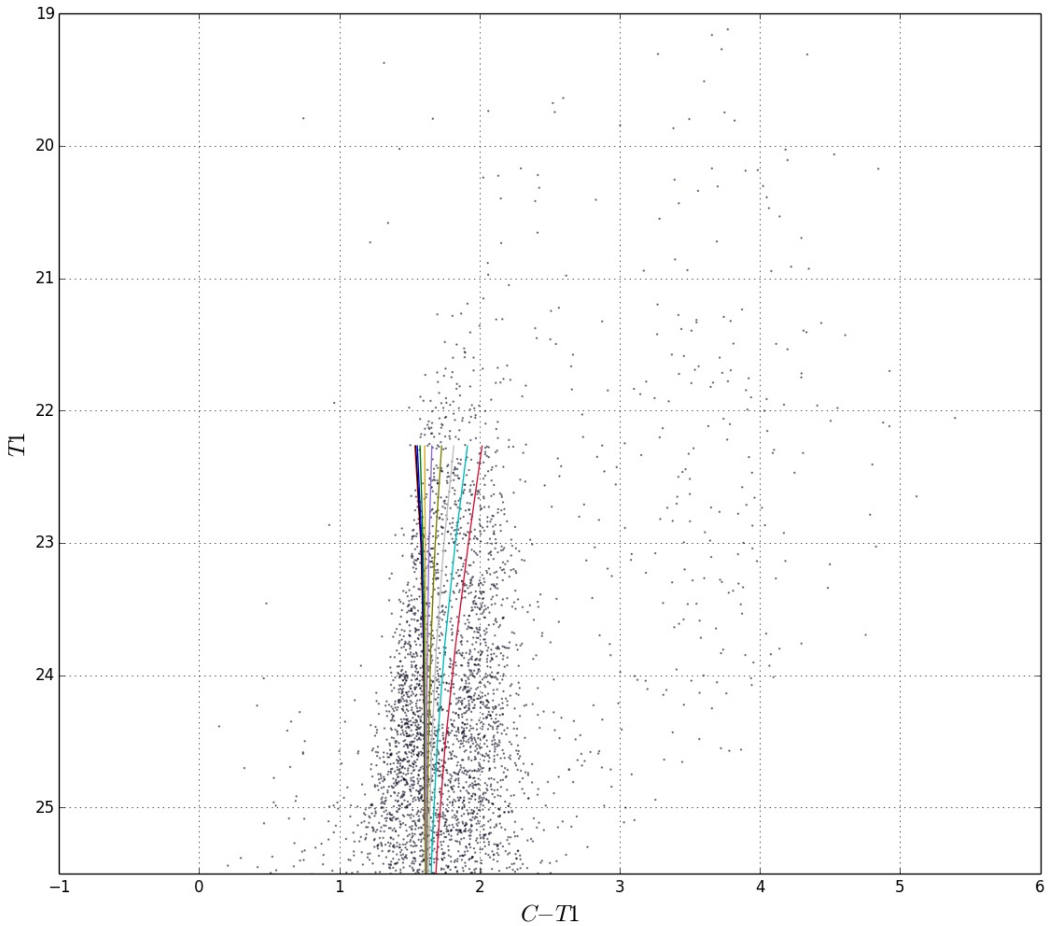

Figure 4.10: NGC 4696 Metal-Poor Mass Accretion Models (metal-poor population). A final metallicity of -0.43 (purple line) had the lowest dispersion error among the different model lines.

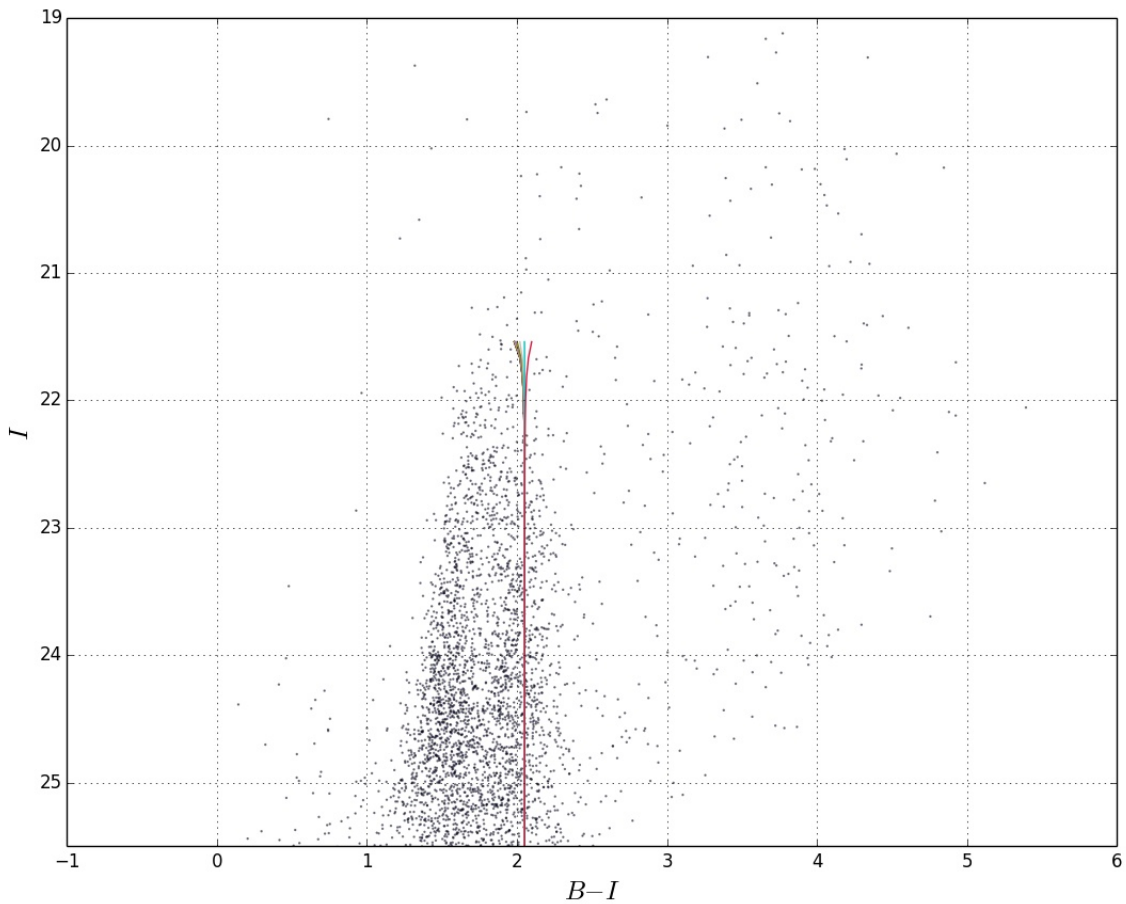

Figure 4.11: NGC 4696 Metal-Rich Metallicity Tracks. All model lines stay close together for the red subpopulation. As seen in the data, there are no significant changes in the metal-rich population.

Chapter 5

Summary

"There is a theory which states that if ever anyone discovers exactly what the Universe is for and why it is here, it will instantly disappear and be replaced by something even more bizarre and inexplicable. There is another theory which states that this has already happened."
- Douglas Adams, *The Hitchhiker's Guide to the Galaxy*

Deep C and R photometry using the CTIO 4m telescope was done in the massive elliptical galaxy, M49, located in the Virgo cluster. The main results of this study are listed below:

- The GCS of M49 shows a very clear color-bimodality in its (C-T1) color distributions.

- The peak colors of the blue, metal-poor subpopulation and the red, metal-rich population were found using a GMM routine developed by Muratov and Gnedin (2010). The peaks were found at 1.27 for the metal-poor clusters and at 1.38 for the metal-rich clusters.

- The blue subpopulation is significantly more populated than the red subpopulation, 1718 objects vs. 689 objects.

- The GCS of M49 does not exhibit a clear MMR slope. This agrees with previous results on M49.

- While self-enrichment is still a possible mechanism to produce a MMR, we attempted a new approach to explain the observed behavior. Self-enrichment predicts that all galaxies should have a similar MMR slope, but the observed data suggests otherwise. Maxwell et al. (2014b) put forward a new mechanism to explain subpopulations of clusters in dwarf galaxies. We have used their basic assumptions and applied to the GCS of elliptical galaxies. The modelling shows that depending on how massive the cluster is and how metal-rich the cloud it accretes material from the faster the change in the cluster's metallicity.

- The modelling does not show any significant changes in the metal-rich subpopulation. The latter is not a surprising result since these clusters started their orbits already enriched and any small addition will not have a strong impact in the resulting globular cluster.

- The mass of the cluster and the metallicity of the surrounding gas are the most influential parameters in the mass accretion scenario. The velocity also plays a role. Too small a velocity and the accreted mass becomes abnormally big. Using Python-based tools, the smallest velocity attainable was 20km/s. A larger velocity would need a higher mass cluster in order to show any significant metallicity changes.

- More tests, especially for other massive elliptical galaxies and even bright spiral galaxies, would be essential in constraining the parameters used in this model and to conduct a comparative study among the different MMR scenarios.

Chapter 6

Acknowledgements

"So long, and thanks for all the fish."

- Douglas Adams, *The Hitchhiker's Guide to the Galaxy*

Many thanks to my adviser Bill Harris for his outstanding mentoring and for sharing with me part of his boundless knowledge of astronomy. Without his precious help, this thesis would not have been possible. I want to thank my thesis committee, Dr. Laura Parker and Dr. Alison Sills for their insightful comments. Many, many thanks are due to the entire staff of the Department of Physics and Astronomy for the many kindness shown to me over the past two years.

I would also like to thank my office-mates and ex-officemates, I appreciated every coffee break in their company.

Finally, I want to thank my parents, Mahmoud and Maria, who happened to visit during the busiest time of this whole project. Your presence was comforting and your cooking simply the best; thanks for your endless support.

References

Ashman, K. M., Bird, C. M., & Zepf, S. E. (1994, December). Detecting bimodality in astronomical datasets. , *108*, 2348-2361. doi: 10.1086/117248

Ashman, K. M., & Zepf, S. E. (1992, September). Globular Clusters, Mergers, and Galaxy Evolution. In *American astronomical society meeting abstracts* (Vol. 24, p. 1186).

Bailin, J., & Harris, W. E. (2009, April). Stochastic Self-Enrichment, Pre-Enrichment, and the Formation of Globular Clusters. , *695*, 1082-1093. doi: 10.1088/0004-637X/695/2/1082

Barmby, P. (2000, December). Globular cluster ages and the formation of M31. In *American astronomical society meeting abstracts* (Vol. 32, p. 1440).

Bekki, K., Campbell, S. W., Lattanzio, J. C., & Norris, J. E. (2007, May). Origin of abundance inhomogeneity in globular clusters. , *377*, 335-351. doi: 10.1111/j.1365-2966.2007.11606.x

Bica, E., Dottori, H., Rodrigues de Oliveira Filho, I., Ortolani, S., & Barbuy, B. (1997, June). Capture of Field Stars by Globular Clusters in Dense Bulge Regions. , *482*, L49-L51. doi: 10.1086/310670

Blakeslee, J. P., Cantiello, M., & Peng, E. W. (2010, February). The Mass-Metallicity Relation of Globular Clusters in the Context of Nonlinear Color-Metallicty Relations. , *710*, 51-63. doi: 10.1088/0004-637X/710/1/51

Bondi, H., & Hoyle, F. (1944). On the mechanism of accretion by stars. , *104*, 273.

Brodie, J. P., & Strader, J. (2006a, September). Extragalactic Globular Clusters and Galaxy Formation. , *44*, 193-267. doi: 10.1146/annurev.astro.44.051905.092441

Brodie, J. P., & Strader, J. (2006b, September). Extragalactic Globular Clusters and Galaxy Formation. , *44*, 193-267. doi: 10.1146/annurev.astro.44.051905.092441

Brodie, J. P., Strader, J., Denicoló, G., Beasley, M. A., Cenarro, A. J., Larsen, S. S., ... Forbes, D. A. (2005, June). Old Globular Clusters Masquerading as Young in NGC 4365? , *129*, 2643-2653. doi: 10.1086/429889

Brodie, J. P., Usher, C., Conroy, C., Strader, J., Arnold, J. A., Forbes, D. A., & Romanowsky, A. J. (2012, November). The SLUGGS Survey: NGC 3115, A Critical Test Case for Metallicity Bimodality in Globular Cluster Systems. , *759*, L33. doi: 10.1088/2041-8205/759/2/L33

Bromm, V., & Clarke, C. J. (2002, February). The Formation of the First Globular Clusters in Dwarf Galaxies before the Epoch of Reionization. , *566*, L1-L4. doi: 10.1086/339440

Cenarro, A. J., Beasley, M. A., Strader, J., Brodie, J. P., & Forbes, D. A. (2007, July). Stellar Populations of Globular Clusters in the Elliptical Galaxy NGC 1407. , *134*, 391-410. doi: 10.1086/518504

Cohen, J. G., & Blakeslee, J. P. (1998, June). An Old Cluster in NGC 6822. , *115*, 2356-2358. doi: 10.1086/300389

Cohen, J. G., Blakeslee, J. P., & Côté, P. (2003, August). The Ages and Abundances of a Sample of Globular Clusters in M49 (NGC 4472). , *592*, 866-883. doi: 10.1086/375865

Conroy, C., & Spergel, D. N. (2011, January). On the Formation of Multiple Stellar Populations in Globular Clusters. , *726*, 36. doi: 10.1088/0004-637X/726/1/36

Côté, P., Marzke, R. O., & West, M. J. (1998, July). The Formation of Giant Elliptical Galaxies and Their Globular Cluster Systems. , *501*, 554-570. doi: 10.1086/305838

Couture, J., Harris, W. E., & Allwright, J. W. B. (1990, August). BVI photometry of globular clusters in M87. , *73*, 671-683. doi: 10.1086/191484

Faber, S. M., Wegner, G., Burstein, D., Davies, R. L., Dressler, A., Lynden-Bell, D., & Terlevich, R. J. (1989, April). Spectroscopy and photometry of elliptical galaxies. VI - Sample selection and data summary. , *69*, 763-808. doi: 10.1086/191327

Forbes, D. A., Brodie, J. P., & Grillmair, C. J. (1997, May). On the Origin of Globular Clusters in Elliptical and cD Galaxies. , *113*, 1652. doi: 10.1086/118382

Forbes, D. A., & Forte, J. C. (2001, April). The connection between globular cluster systems and the host galaxies. , *322*, 257-261. doi: 10.1046/j.1365-8711.2001.04052.x

Forbes, D. A., Grillmair, C. J., Williger, G. M., Elson, R. A. W., & Brodie, J. P. (1998, January). HST imaging of the globular clusters in the Fornax cluster - NGC 1399 and NGC 1404. , *293*, 325. doi: 10.1046/j.1365-8711.1998.01202.x

Forbes, D. A., Spitler, L. R., Harris, W. E., Bailin, J., Strader, J., Brodie, J. P., & Larsen, S. S. (2010, September). VizieR Online Data Catalog: Candidate globular clusters in NGC 5170 (Forbes+, 2010). *VizieR Online Data Catalog*, *740*, 30429.

Geisler, D., Lee, M. G., & Kim, E. (1996, April). Washington Photometry of the Globular Cluster System of NGC 4472.I.Analysis of the Metallicities. , *111*, 1529. doi: 10.1086/117894

Harris, G. L. H., Geisler, D., Harris, H. C., & Hesser, J. E. (1992, August). Metal abundances from Washington photometry of globular clusters in NGC 5128. , *104*, 613-626. doi: 10.1086/116259

Harris, W. E. (1996, October). A Catalog of Parameters for Globular Clusters in the Milky Way. , *112*, 1487. doi: 10.1086/118116

Harris, W. E. (2009, July). Globular Cluster Systems in Giant Ellipticals: The Mass/Metallicity Relation. , *699*, 254-280. doi: 10.1088/0004-637X/699/1/254

Harris, W. E., Harris, G. L., & Hudson, M. J. (2015, June). Dark Matter Halos in Galaxies and Globular Cluster Populations. II. Metallicity and Morphology. , *806*, 36. doi: 10.1088/0004-637X/806/1/36

Harris, W. E., & Harris, G. L. H. (2002, June). The Halo Stars in NGC 5128. III. An Inner Halo Field and the Metallicity Distribution. , *123*, 3108-3123. doi: 10.1086/340466

Harris, W. E., Harris, G. L. H., & Alessi, M. (2013, August). A Catalog of Globular Cluster Systems: What Determines the Size of a Galaxy's Globular Cluster Population? , *772*, 82. doi: 10.1088/0004-637X/772/2/82

Harris, W. E., Spitler, L. R., Forbes, D. A., & Bailin, J. (2010, January). Diamonds on the Hat: globular clusters in the Sombrero galaxy (M104). , *401*, 1965-1982. doi: 10.1111/j.1365-2966.2009.15783.x

Harris, W. E., Whitmore, B. C., Karakla, D., Okoń, W., Baum, W. A., Hanes, D. A., & Kavelaars, J. J. (2006, January). Globular Cluster Systems in Brightest Cluster Galaxies: Bimodal Metallicity Distributions and the Nature of the High-Luminosity Clusters. , *636*, 90-114. doi: 10.1086/498058

Hirschi, R. (2007, April). The Evolution of Massive Stars in the Context of V838 Monocerotis. In R. L. M. Corradi & U. Munari (Eds.), *The nature of v838 mon and its light echo* (Vol. 363, p. 257).

Kim, S., Yoon, S.-J., Chung, C., Caldwell, N., Schiavon, R. P., Kang, Y., … Lee, Y.-W. (2013, May). Nonlinear Color-Metallicity Relations of Globular Clusters. V. Nonlinear Absorption-line Index versus Metallicity Relations and Bimodal Index Distributions of M31 Globular Clusters. , *768*, 138. doi: 10.1088/0004-637X/768/2/138

Kissler-Patig, M., Kohle, S., Hilker, M., Richtler, T., Infante, L., & Quintana, H. (1997, March). Globular cluster systems of early-type galaxies in Fornax. , *319*, 470-480.

Kundu, A. (2008, September). Observational Biases Masquerading as Cosmological Effects? a Cautionary tale about Blue Tilts and Other Trends in Globular

Cluster Systems. , *136*, 1013-1029. doi: 10.1088/0004-6256/136/3/1013

Li, H., & Gnedin, O. Y. (2014, November). Modeling the Formation of Globular Cluster Systems in the Virgo Cluster. , *796*, 10. doi: 10.1088/0004-637X/796/1/10

Maxwell, A. J., Wadsley, J., Couchman, H. M. P., & Sills, A. (2014a, April). The Celestial Buffet: multiple populations and globular cluster formation in dwarf galaxies. , *439*, 2043-2049. doi: 10.1093/mnras/stu086

Maxwell, A. J., Wadsley, J., Couchman, H. M. P., & Sills, A. (2014b, April). The Celestial Buffet: multiple populations and globular cluster formation in dwarf galaxies. , *439*, 2043-2049. doi: 10.1093/mnras/stu086

McKee, C. F., & Ostriker, J. P. (1977, November). A theory of the interstellar medium - Three components regulated by supernova explosions in an inhomogeneous substrate. , *218*, 148-169. doi: 10.1086/155667

Mieske, S., & Baumgardt, H. (2007, December). On the efficiency of field star capture by star clusters. , *475*, 851-857. doi: 10.1051/0004-6361:20078450

Mieske, S., Jordán, A., Côté, P., Kissler-Patig, M., Peng, E. W., Ferrarese, L., … West, M. J. (2006, December). The ACS Virgo Cluster Survey. XIV. Analysis of Color-Magnitude Relations in Globular Cluster Systems. , *653*, 193-206. doi: 10.1086/508986

Mieske, S., Jordán, A., Côté, P., Peng, E. W., Ferrarese, L., Blakeslee, J. P., … West, M. J. (2010, February). The ACS Fornax Cluster Survey. IX. The Color-Magnitude Relation of Globular Cluster Systems. , *710*, 1672-1682. doi: 10.1088/0004-637X/710/2/1672

Muratov, A. L., & Gnedin, O. Y. (2010, August). Modeling the Metallicity Distribution of Globular Clusters. , *718*, 1266-1288. doi: 10.1088/0004-637X/718/2/1266

Peng, E. W., Jordán, A., Côté, P., Blakeslee, J. P., Ferrarese, L., Mei, S., … Tonry, J. L. (2006, March). The ACS Virgo Cluster Survey. IX. The Color Distributions of Globular Cluster Systems in Early-Type Galaxies. , *639*, 95-119. doi: 10.1086/498210

Puzia, T. H., Kissler-Patig, M., Brodie, J. P., & Huchra, J. P. (1999, December). The Age Difference between the Globular Cluster Subpopulations in NGC 4472. , *118*, 2734-2750. doi: 10.1086/301141

Puzia, T. H., Kissler-Patig, M., & Goudfrooij, P. (2005, December). Extremely α -Enriched Globular Clusters in Early-Type Galaxies. In *American astronomical society meeting abstracts* (Vol. 37, p. 1319).

Recchi, S., & Danziger, I. J. (2005, June). Self-enrichment in globular clusters. I. An analytic approach. , *436*, 145-154. doi: 10.1051/0004-6361:20042275

Secker, J. (1992, October). A statistical investigation into the shape of the globular cluster luminosity distribution. , *104*, 1472-1481. doi: 10.1086/116332

Spitler, L. R., Larsen, S. S., Strader, J., Brodie, J. P., Forbes, D. A., & Beasley, M. A. (2006, October). Hubble Space Telescope ACS Wide-Field Photometry of the Sombrero Galaxy Globular Cluster System. , *132*, 1593-1609. doi: 10.1086/507328

Strader, J., Beasley, M. A., & Brodie, J. P. (2007, May). Globular Cluster Metallicity Subpopulations in NGC 4472. , *133*, 2015-2019. doi: 10.1086/512770

Strader, J., Brodie, J. P., Spitler, L., & Beasley, M. A. (2006, December). Globular Clusters in Virgo Ellipticals: Unexpected Results for Giants and Dwarfs from Advanced Camera for Surveys Imaging. , *132*, 2333-2345. doi: 10.1086/509124

Strader, J., & Smith, G. H. (2008, November). The Origin of the Blue Tilt in Extragalactic Globular Cluster Systems. , *136*, 1828-1836. doi: 10.1088/0004-6256/136/5/1828

Webb, J. J., Sills, A., & Harris, W. E. (2013, December). Globular Cluster Scale Sizes in Giant Galaxies: The Case of M87 and the Role of Orbital Anisotropy and Tidal Filling. , *779*, 94. doi: 10.1088/0004-637X/779/2/94

Woitke, P. (2006, December). Too little radiation pressure on dust in the winds of oxygen-rich AGB stars. , *460*, L9-L12. doi: 10.1051/0004-6361:20066322

Woodley, K. A., & Harris, W. E. (2011, January). Possible Subgroups of Globular Clusters and Planetary Nebulae in NGC 5128. , *141*, 27. doi: 10.1088/0004-

6256/141/1/27

Woodley, K. A., Harris, W. E., Puzia, T. H., Gómez, M., Harris, G. L. H., & Geisler, D. (2010, January). The Ages, Metallicities, and Alpha Element Enhancements of Globular Clusters in the Elliptical NGC 5128: A Homogeneous Spectroscopic Study with Gemini/Gemini Multi-Object Spectrograph. , *708*, 1335-1356. doi: 10.1088/0004-637X/708/2/1335

Worthey, G. (1994, November). Comprehensive stellar population models and the disentanglement of age and metallicity effects. , *95*, 107-149. doi: 10.1086/192096

Yoon, S.-J., Lee, S.-Y., Yi, S., & Lee, Y.-W. (2006, June). On the Origin of Bimodal Color Distribution of Globular Clusters in Early-type Galaxies. In *American astronomical society meeting abstracts #207* (Vol. 207, p. 128.22).

Zinn, R. (1985, June). The globular cluster system of the galaxy. IV - The halo and disk subsystems. , *293*, 424-444. doi: 10.1086/163249